Upslope migrating sand waves on sediment-starved shelves: an example from the southeastern continental margin of the Korean Peninsula

Deniz Cukur[1,*], Gee-Soo Kong[1], David M. Buchs[2], Gwang-Soo Lee[1], Seong-Pil Kim[1], In-Kwon Um[1], Jong-Hwa Chun[1], Byoung-Yeop Kim[1], Ji Eun Seo[3], Hyun Sook Chae[3], Senay Horozal[4]

[1]Petroleum and Marine Research Div., Korea Institute of Geoscience and Mineral Resources (KIGAM), 124 Gwahak-ro, Yuseoung-gu, Daejeon 34132, Republic of Korea

[2]School of Earth and Ocean Sciences, Cardiff University, UK

[3]Woosuk University, Dept. of Life Science, Jincheon 27841, Republic of Korea

[4]Chungnam National University, Daejeon, Republic of Korea

Corresponding author: Dr. Deniz Cukur

Email: dcukur@kigam.re.kr

Abstract

An uncharted field of sand waves was discovered in a low-relief submarine canyon incised in the outer shelf on the southeastern continental margin of the Korean Peninsula in water depths of 180 to 190 m. We characterize the nature and origin of the waves and the sand forming them using sub-bottom chirp profiles, eXpendable bathythermograph (XBT) profile, multibeam echosounder (MBES) data, and sediment samples from four piston cores. Two types of sand waves characterized by distinct height versus wavelength relationships were found in the study area. The sand waves in the upper, narrower part of the shelf-incised canyon are sinuous-crested, with amplitudes of 0.3 m to 2.1 m (mean: ~1 m) and wavelengths of 10 to 45 m (mean: ~24 m). Their asymmetry indicates migration upslope in a southwesterly direction, opposite to the surface currents. In contrast, the lower part of the canyon that is wider and closer to the margin of the continental shelf hosts nine long (ca. 1 km) curvilinear-crested sand waves with symmetrical crests; these waves likely reflect transient bedforms forming under fluctuating current conditions.

The sediment of the sand waves consists of a variable mixture of siliciclastic and carbonate materials. The carbonate fraction (~22–55%; mean: ~34%) is derived mainly from the remains of bryozoans, bivalves, echinoderms, foraminifers, gastropods, and serpulids. Six bioclasts were dated by the radiocarbon method between ca. 41.3 and 11.8 ka BP. These relatively old ages and palaeontological data supports reworking from a shallow-marine environment during the last glacial transgression and limited sedimentation/sediment supply in the study area. The siliciclastic fraction (~44–79%; mean: ~37%) is composed of rounded to subrounded quartz and feldspar of moderate to good sorting and a mean grain size of ~1.3 phi (medium sand). The uppermost ~30 cm of all the sand wave cores reveals a decrease in the grain size of the siliciclastic fraction coupled with an increase in the carbonate/siliciclastic ratio, suggesting episodic sediment reworking and migration of the sand waves in response to fluctuating bottom currents. The coarser sediment that forms the core of the sand waves records bedload transport during periods of stronger currents. Finer carbonate-rich pelagic sediment (i.e., plankton) accumulated at the top of the sand waves during periods of weaker bottom

currents. Significantly, our results show that the grain size and mineralogy of the sediment composing the sand waves are controlled by changes in hydrodynamic conditions. Our study provides novel geomorphological evidence for the influence of SW-flowing cold-water incursions (Korean Strait Bottom Cold Water) on the seafloor sediments.

Keywords: sand waves, bottom currents, piston cores, submarine canyon, southeastern shelf of Korea

1. Introduction

Sand waves (sometimes referred to as megaripples or sand dunes) are large-scale sedimentary bedforms common on many continental shelves worldwide (e.g., Ashley, 1990; Flemming, 1980; Viana et al., 1998; Wynn and Stow, 2002; Stow et al., 2009). They typically form in response to strong tidal, geostrophic or storm-driven currents, and are generally sinuous crested in plan view and asymmetrical in cross-section with a steeper, shorter lee side (downstream), and more gentle, longer stoss side (facing upstream) (Wynn and Stow, 2002). Smaller sand waves have wave heights of only 3–5 cm, while medium-sized and larger sand waves are as high as up to a few meters to tens of meters (Ye Yincan et al., 2017). Factors that control their development include local variations in topography, availability of sand and coarser sediments, hydrodynamic regime, and global variations in climate and sea level (Viana et al. 1998; Flemming, 2000). The dynamic nature of sand waves can make them hazardous to submarine installations, with typical effects including destabilizing underwater drilling platforms and moorings or causing free spans in pipelines (Belde et al., 2017). Migrating sand waves can also cover submarine mines and chemical waste, which may lie hidden within the seafloor and become exposed in the future (Nemeth et al., 2002). Moreover, understanding the formation and evolution of coarse-grained bedforms can provide useful information for paleoceanographic reconstructions and hydrocarbon exploration (Hernandez-Molina et al., 2017).

The advent of recent high-resolution marine geophysical surveys supplemented by modeling has revealed a wide variety of sand wave occurrence, with distinct dimensions, geometries, and mobility (e.g., Ernstsen et al., 2006). Well studied locations of sand or sediment waves on continental shelves include those in the Gulf of Valencia (Albarracín et al. 2014), on the western Grand Banks of Newfoundland (Dalrymple et al., 1992), on the southeast African continental shelf (Flemming, 1980), on the Australian Northwest Shelf (Belde et al., 2017), in the southern Taiwan Strait (Zhou et al., 2020), Irish Sea (Van Landeghem et al., 2009), and on the southern Ebro continental shelf (Lo Iacono et al., 2010 > 116 m). However, most of these studies are focused on shallow-marine environments (water depths < 130 m) where tides, waves, storms, and coastal currents influence bedform generation. As a result, relatively little is known about the nature of bedforms produced by deep-water bottom currents. Moreover, well-documented examples of sand waves from deep waters remain relatively limited, mainly due to the poor resolution of geophysical data (i.e., seismic and multibeam echosounder data) and the difficulty in recovering sediment cores. Locations of deep water (> 130 m) sand waves on outer continental shelves include the northern South China Sea (Reeder et al., 2011; Ma et al., 2019; Zhang et al., 2019), the NE Atlantic (Lo Iacono et al., 2020), offshore northern Norway (Bøe et al., 2009, 2015), and on the upper continental slope of the Mozambique margin (Miramontes et al., 2020). In the absence of strong tidal currents and waves, the formation of subaqueous sand waves and dunes on the outer continental margins has been related to unidirectional flows produced by ocean currents (Ikehara and Kinoshita, 1994; Kubo et al.,

2004), by strong geostrophic currents along the shelf-break (Lo Iacono et al., 2010; King et al., 2014; Bøe et al., 2015), or by internal waves (Ma et al., 2016; Droghei et al., 2016; Miramontes et al., 2020). The local topographic constrictions (i.e., narrowing channels and depressions) are suggested to locally play a crucial role in accelerating bottom currents and favoring the formation of large sand waves (Kubo et al., 2004; Barrie et al., 2009; Lo Iacono et al., 2010; Rovere et al., 2019).

No sand waves have to date been reported from the southeastern continental shelf of Korea. Most of the previous work in and adjacent to the study area focused on the oceanographic data supporting the presence of a southwestward flowing cold undercurrent, namely the Korea Strait Bottom Cold Water Current (KSBCW) along the outer shelf and upper continental slope. Shin et al. (2006) have assembled instrumental observations suggesting a general southward directed cold, ca. 25 cm/s fast, bottom current near our study area (See Fig. 1A for their Acoustic Doppler Current Profiler (ADCP) line). The persistent southward flow is also confirmed by Lee and Kim (2016), suggesting near-bottom velocities of 24 cm/s at a water depth of 100–124 m. However, geomorphologic evidence supporting sand transportation in response to such bottom currents remains to be provided.

This paper presents the discovery of sand waves on the outer southeastern continental shelf of the Korean Peninsula (Fig. 1A-B). We integrate multibeam echosounder (MBES) data, subbottom chirp profiler, an XBT profile, and four piston cores to (1) document the morphology of the sand waves, (2) describe the composition, grain size, and texture of the sediment, and (3) constrain hydrodynamic processes associated with their formation. Our observations indicate that bottom currents have been active in recent years to affect sediment distribution and generate SW-migrating sand waves within a submarine canyon incised into the outer shelf. In the present study, the nomenclature of transverse bedforms was coined by Stow et al. (2009). We use the term sand wave to refer to subaqueous, transverse bedforms of sand that have amplitudes of 0.3–3 m and wavelengths of 10–140 m, whereas the smaller, superimposed bedforms on their tops (wavelengths < 20 m and heights < 0.5 m) are referred to as dunes.

2. Regional and oceanographic setting

The southeastern continental shelf of Korea occupies the southwestern margin of the East Sea (Fig. 1A). The broad shelf is as wide as 250 km, covers an area of 4300 km^2, and is bounded to the north by the Ulleung Basin, to the southwest by the Korea Trough, and the southeast by the Japanese Islands (Fig. 1A). Water depths on the gently (0.03°) seaward-sloping shelf range from 100–200 m, and the shelf edge is at water depths of 200–300 m (Fig. 1B). Prominent geomorphic features of the shelf include giant crescent-shaped depressions, the head of a submarine canyon, and exposed basement highs (Fig. 1B). Our study area is located on the floor of a submarine canyon incised into the outer shelf (Fig. 1B). The northeast-trending canyon head is about 40 km long, 8 km wide, and 50 m deep (Fig. 1C-D).

The late Quaternary evolution of the shelf is characterized by a fluctuating climate and sea level, which are reflected in seabed sediments and geomorphic features (Park et al., 2000; Koo et al., 2014; Horozal et al., 2021). During the Last Glacial Maximum (LGM) at around 20 ka BP, sea level was ~120–130 m lower than present (Stanford et al., 2011; Park et al., 2000), leading to subaerial exposure of major parts of the shelf. However, the present-day water depths (180–190 m) and limited tectonic activity in our study area suggest that the outer shelf was not emergent and occupied a relatiely shallow marine environment during the LGM. The

postglacial transgression began about 15 ka BP, eventually submerging the entire shelf as sea level rose to its present elevation (Park et al., 2000).

Sediment texture and composition on the southeastern continental shelf of Korea vary spatially with increasing water depth (Koo et al., 2014). Extensive clay-rich terrigenous muddy sediments, named as the Korea Strait shelf mud (KSSM; Chun et al., 2015), occur above 100 m on the inner shelf parallel to the coastline. In contrast, the outer shelf is mainly covered by coarser relict sediments that are thought to have been deposited during lowstand sea level (Koo et al., 2014). These coarse-grained relict sediments are dominated by (fossil) carbonate fragments with a bulk composition of 10–60% (Chun et al., 1999). Holocene terrigenous clay-rich sediment, much of which is trapped within coastal depositional environments, is derived from nearby large river systems (i.e., Seomjing and Nakdong Rivers) (Park et al., 1996).

The Korea Strait, which is about 140 km wide with an average depth of ~100 m, connects the East Sea with the East China Sea (Fig. 1A). The Tsushima Warm Water (TWW) flows northeastward through the Korea Strait into the East Sea, supplying warm and saline surface water (Na et al., 2010). The TWW splits into two branches near Tsushima Island; one branch flows along the Korean coast, and the other flows along the Japanese coast (Fig. 1A; Cho and Kim, 1999). The Korea Strait Bottom Cold Water (KSBCW) forms a deep countercurrent, flowing southeastward along the Korean shelf margin (Fig. 1A; Cho and Kim, 1998; Chang et al., 2004; Takikawa et al., 2005; Shin et al., 2006; Lee and Kim, 2016). The KSBCW usually intrudes between the surface and bottom layers and reaches a maximum speed of 25 cm/s (Shin et al., 2006; Lee and Kim, 2016). It is usually defined as a water mass with a temperature of less than 10 °C that appears only in the western channel of the Korea Strait (Cho and Kim, 1998). Kim et al. (2006) showed that the KSBCW flows southward within 70 km of the Korean coast from May to January, and Min et al. (2006) documented interannual KSBCW variability. KSBCW water originates as East Sea Intermediate Water (Cho and Kim, 1998; Yun et al., 2004). Based on 35 years of temperature data, Na et al. (2010), show that the interannual KSBCW variability is closely linked with water temperature variability in the southwestern region of the East Sea at about 50–100 m depth. Park et al. (1995), based on a hydraulic model, suggested that the sloping seafloor between the Korea Trough and the southwestern upper slope of the Ulleung Basin induces the southwestward flow of cold water onto the shelf.

The tidal range within the southeastern continental shelf of Korea is typically low (< 1 m), with tidal current velocities ranging between 18–27 cm/s (Teague et al., 2001, 2006). The tidal range increases towards to as much as 3 m in the southwestern part of the Korea Strait where current velocities reach 13–23 cm/s. Peak non-tidal currents vary spatially along the margin, exceeding 30 cm/s in the middle of the Korea Strait (Teague et al., 2001). Strong typhoons originating from the northwestern Pacific Ocean are common in the Korean Peninsula (Choi et al., 2012) and are significant agents in sediment movement and deposition (Chun et al., 2015).

3. Datasets and methods

Data used in this study consist of (1) approximately 250 km^2 of multibeam echosounder (MBES) data, (2) ~10 km of chirp-generated subbottom profiles, (3) an Expendable BathyThermograph (XBT) profile, and (4) four piston cores collected from different parts of the sand wave field (Fig. 1B). All datasets presented in this study were acquired by the *R/V*

Tamhae II of the Korea Institute of Geosciences and Mineral Resources (KIGAM). MBES data were collected in 2019 using a Kongsberg EM 302 multibeam echosounder with a nominal frequency of 30 kHz and a swath width of 130 m. These data were processed with CARIS HIPS and SIPS hydrographic data processing software with a horizontal spatial resolution of 2 m. The subbottom chirp profiler data were acquired in 2020 using an SYQWEST-BATHY 2010 subbottom profiler system. The chirp system can deliver up to 8 cm of vertical resolution with bottom penetration up to 300 meters.

Four piston cores were collected in 2020 in different parts of the sand wave field (Fig. 1B). The cores were split, photographed, and described at the KIGAM laboratory. For grain size analysis, we collected samples of ca. 10 g at intervals of 20 cm; the samples were then freeze-dried. The representative samples were treated with 10% H_2O_2 at 60 °C for 10 hours and 2 N HCl for 3 hours to remove the organic matter and biogenic carbonate, respectively. The grain size of the residues was determined with a Microtrac S3500 laser particle analyzer. Grain-size distribution and textural parameters of the remaining siliciclastic fraction were calculated using the graphic percentile method described by Folk and Ward (1957).

Quantitative analyses of key mineral assemblages were determined at KIGAM by X-ray powder diffraction (XRD) and computer software (SIROQUANT) based on the Rietveld quantification method. For the XRD analysis, a Philips X'pert MPD diffractometer was used. Sixteen samples of bulk sediment were selected based on proximity to intervals sampled for grain size analysis. The samples were collected in cores 20IH-P10, 20IH-P11, and 20IH-P13 to document the lateral variability of mineral composition of sand waves throughout the study area.

We obtained six ^{14}C date of well-preserved fossils at the KIGAM AMS laboratory (Table 1). Palaeontological analysis of fossils provides additional constraints on water depth and ecology during deposition.

We assumed that the observed sand waves are in an equilibrium state, then estimated flow conditions using the threshold equation for the occurrence of sand waves:

$$\frac{U_* D}{\nu} = 1.117 \left(\frac{g D^3}{\nu^2}\right)^{1/2} - 2.087 \qquad (1)$$

where U* is the shear velocity, D the grain size, ν the kinematic viscosity (which was taken as 1.73E-6 m^2/s for seawater at 2 ºC temperature; ITTC – Recommended Procedures; 2011), and g the acceleration due to gravity (Allen 1972; Allen and Homewood 1984; Kubo et al., 2004). Based on the core sediment samples, we determined grain sizes of 0.38 mm and 0.45 mm for minimum and maximum values. We then estimated shear velocity by assuming a logarithmic velocity profile for turbulent flow:

$$V(z) = \frac{U_*}{K} \ln \frac{z}{z_0} \qquad (2)$$

where $V(z)$ is the flow velocity at height z above the bed, K the von Karman's coefficient ($K \approx 0.4$), z is the height above the bed corresponding to the water depth, and z_0 is the roughness length (i.e., the hypothetical distance from the bed where the logarithmic velocity profile equals zero). The distance z_0 depends on the bed roughness. Assuming a hydraulically smooth flow, z_0 is estimated as:

$$z_0 \approx \nu / 9U_* \qquad (3)$$

over an initially flatbed (Julien 1998). Once sand waves or dunes are present, the bed is no

longer flat, and the roughness will depend more on the bedform dimension than on grain size (Kubo et al., 2004). Wooding et al. (1973) estimated the roughness of the bed covered by bedwaves as:

$$z_0 = 2H \left(\frac{H}{L}\right)^{1.4} \quad (4)$$

where H is the height and L is the wavelength of the bedforms.

4. Results

4.1 Sand wave distribution and geometry

From MBES data we identified at least 110 individual sand waves on the floor of the submarine canyon at water depths of 180 to 190 m (Fig. 2). The sand waves in the southwest of the study area are sinuous-crested and asymmetrical, with the lee side facing SW (Fig. 3). For each sand wave we determined the height, wavelength, and leeward slope angle (statistics are presented in Table 2). The heights of the sinuous-crested sand waves range from 0.3 m to 2.1 m (mean: ~1 m), and wavelengths range from 10 to 45 m (mean: ~24 m; Fig. 4). The MBES data reveal that the amplitudes of the sand waves are smaller in the NE, becoming larger and more pronounced towards the SW, but subdued again towards the SW end of the sand wave field (Figs. 2 and 4).

A distinct set of large curvilinear-crested sand waves occurs to the northeast of the sinuous-crested ones (Figs. 2 and 5). These have N-S trending curvilinear crests with a length of ca.1 km (Fig. 5). Their heights and wavelengths range from 1–2.7 m (mean: 2 m) and 60–140 m (mean: 100 m), respectively, with their crests generally spaced between 10–150 m apart. Smaller dune sets with wavelengths of 10–20 m and heights of 0.2–0.5 m are superimposed on the tops or slopes of the curvilinear sand waves (Fig. 5). The MBES data also reveal several bathymetric highs and irregularly shaped depressions of up to 20 m deep and 1,000 m^2 in area that occur locally at the SW corner of the study area (Fig. 2).

Following Flemming (2000), we investigated the relationship between the height (h) and wavelength (λ) of the sand waves (Fig. 6A). There is a good correlation between h and λ for the sinuous-crested sand waves (r=60); the heights notably increase with increasing wavelength. Correlation between λ and h is also observed for the curvilinear-crested sand waves, albeit with a lower correlation coefficient (r=40). Figure 6A shows that all of the sand waves in the study area plot below the global maximum h vs λ relationship (Flemming, 1998, 2000); for h < 0.4 m, the sinuous-crested sand waves plot below the global mean. The relationship between λ and h clearly confirms that the sinuous-crested and curvilinear-crested sand waves have distinct geometries. Notably, the h/λ ratio of the sinuous crested sand-waves is > 0.03 while that of curvilinear crested sand waves is < 0.03 (Fig. 6B)

A clear relationship between height and lee side slope of the sinuous-crested sand waves is also observed (r=0.60, Fig. 6C). The general trend shows that the slope of the lee side increases with height but never exceeds ~20°. In contrast, no clear link between slope and height was observed for the curvilinear-crested sand waves (Fig. 6C).

4.2 Acoustic stratigraphy

A sub-bottom chirp profile traversing the sand waves reveals numerous > 110 distinctive

sand waves that dominate the morphology of the seabed (Fig. 7A). Acoustically, the sand wave seabed is characterized by an undulating high-amplitude reflection. Shallow strata beneath the sand waves are acoustically transparent, consistent with the relatively coarse and homogenous sand-size sediments in the cores (Fig. 8A). In the NE, a distinct subbottom reflector occurs underneath the curvilinear-crested sand waves by parallel to the seabed reflector. It disappears or pinches out near the smaller sand waves and is interpreted as an older hard-ground or an erosional surface.

4.3 Water masses above the sand wave field

An XBT profile through the water column above the sand wave field was collected to characterize the water temperature and distinguish water masses in the study area (Fig. 7B). The temperature profile shows three distinct zones above the seafloor, including surface-, intermediate-, and deep cold-water. The surface water extends down to ~32 m and is characterized by a relatively warm water temperature (> 15 °C). The intermediate water has a lower temperature (> 10 °C) and is separated from the cold water mass (namely KSBCW) at a water depth of 75 m. The XBT data further reveal that the deep cold water is ~100 m thick, and its temperature remains remarkably constant at 1.7 °C (Fig. 7B).

4.4. Sediments characteristics of the sand waves

Four piston cores were collected from the sand waves to characterize the seabed sediments and associated transport and deposition processes (Fig. 2).

4.4.1 Sedimentary facies

The analysis of the cores (Fig. 2) indicates that the sand waves are composed of massive shelly sand containing a mix of siliciclastic and bioclastic grains (MSS; Fig. 8A). The siliciclastic fraction of the sediments is mainly composed of quartz and lesser amounts of feldspars, chert, and iron-oxide minerals (i.e., magnetite or hematite) that is mostly sub-rounded to well-rounded (Fig. 8B). The bioclastic fraction includes the skeletal remains of bivalves, gastropods, benthic and planktonic foraminifers, bryozoans, echinoderms, and serpulids (Fig. 8C–M). Most of the organisms are very well rounded echinoderm fragments (Fig. 8I) with abundant radiole remnants (Fig. 8J) and micropores commonly infilled with silt (Fig. 8K). Boring holes are common in the shells of the bivalves (Fig. 8C–D).

Bryozoans of various forms and colors constitute a high component of the bioclastic fraction of all the samples (Fig. 8G–H) but are particularly common in the topmost samples of the cores. Some are cold-water organisms, whereas others represent warm-water faunas (Table 3). Although rare, serpulids are found in some of the core samples (Fig. 8L–M), where they are commonly attached to bryozoans or gastropods.

4.4.2 Mean grain size, texture, and sorting

Sediment texture in the sand wave field is relatively homogeneous, without a clear distinction between sinuous-crested and curvilinear-crested sand waves (Fig. 9). Sand is the dominant size fraction in all samples, with contents generally ranging from 82 -100% (mean: 98%). Silt is the next most abundant size fraction of the samples (0–18%) but exceeds 10% in

only two samples towards the topmost portions of cores P10 and P11 (Fig. 9). Clay or gravel were not present in our samples.

The calculated mean grain size in the sand wave cores ranges from 1.1 ϕ to 2.7 ϕ with average values of 1.35, 1.16, 1.25, and 1.4 ϕ for the P09, P10, P11, and P13, respectively (Fig. 9). The average mean grain-size is medium sand (Fig. 9). It is noteworthy that finer sand is consistently found in the uppermost part of all retrieved cores.

The average sorting value (~0.57 ϕ) indicates that the sediment in the study area is mostly moderately well sorted (Fig. 9). The values range from 0.59 ϕ to 0.80 ϕ (moderately well sorted to moderately sorted), 0.45–1.13 (well sorted to poorly sorted), 0.44-1.77 ϕ (well sorted to poorly sorted), and 0.46-1.3 ϕ (moderately well sorted to moderately sorted) for the P09, P10, P11, and P13 sediments respectively.

The sorting versus mean grain size plot for all the samples (Fig. 10A) reveals a good linear correlation (r=0.5) with only a few outliers. The correlation is even better (r=0.7) when excluding core P13, which is collected from the curvilinear-crested sand wave field. The sediment from all cores exhibits better sorting in the coarser sizes; sorting decreases as the mean grain size decrease.

To facilitate comparisons among samples from different sites, the grain size parameters of the samples from the four cores are plotted in figure 10B. Although minor, there is a systematic difference in grain size and sorting in each locality. P13 sediment samples, for instance, are the most fine grained, whereas P10 samples are the coarsest. The slightly coarser sediments in P10 and P11 coincide with areas of slightly larger sand waves (Fig. 4). Decreased sorting is also evident in P10 compared to the other cores. The P11 and P10 sediment samples are better sorted than P13 and P09 sediment samples (Fig. 10B).

4.4.3 Mineralogical characteristics

Sixteen samples from cores P13, P10, and P11 were analyzed for mineral composition by XRD (Fig. 11). Overall, the sinuous- and curvilinear-crested sand waves are relatively uniform in mineral composition. The samples contain both siliciclastic (quartz, albite feldspar, and microcline feldspar) and carbonate (calcite, aragonite, dolomite) minerals (Fig. 11). The most dominant mineral in all samples is quartz, ranging between 42–61 weight percent (wt%) (mean: 50 wt%) (Fig. 11). Calcite is the second most abundant mineral (15.6–31.8 wt%; mean: 23 wt%). In the uppermost portion of core P10, calcite forms the most abundant mineral (~40 wt%). The samples are also associated with moderate amounts of aragonite (11.3 to 14.9 wt%; mean: 13 wt%), microcline (6.2 to 10.7 wt%; mean: 8.4 wt%), and low amounts of albite (4.2 to 6.7 wt%; mean: 5.4 wt%). Dolomite (< 1.5 wt%) is also present in the upper part of core P10 (Fig. 11). Magnetite and other opaque minerals are below the XRD detection limits, but traces of these minerals were observed under the microscope in several samples.

4.5 XRD – grain size data integration

We plotted grain size and sorting versus $CaCO_3$ (calcite+aragonite+dolomite) to evaluate possible links between grain size parameters and sediment composition in the sampled sand waves (Fig. 12). The plots show a good correlation between the grain size and sorting and the $CaCO_3$ abundance in the cores (r=0.67). The coarser and more poorly sorted sediment is generally associated with the lower $CaCO_3$ contents. This indicates that the largest particles in

the sand waves are primarily composed of siliciclastic material (i.e., quartz and feldspar), whereas the finest particles (concentrated at the top of the cores) have the highest $CaCO_3$ abundance (microfossils, nannofossils and/or carbonate silt). Small differences in $CaCO_3$ and siliciclastic content are also found between cores exhibiting distinctly different overall grain size (i.e., P10 vs. P11 and P13). Although we have a relatively limited number of samples, these observations consistently support a relationship between the composition and grain size/sorting of the sediment, with a noticeable change in the uppermost part of the sand waves.

4.6 Dating

Five well-preserved bivalves and an echinoderm fragment were dated by accelerator mass spectrometry (AMS) ^{14}C dating to document whether these fossils are old and inherited from a LGM shallow marine environment (before the marine transgression) or are recent organisms deposited in deeper marine conditions. The bivalves yielded ages of 41325 ± 425 yr BP, 37723 ± 328 yr BP, 35653 ± 270 yr BP, 35276 ± 289 yr BP, and 12123 ± 52 yr BP (Table 1), while the echinoderm fragment yielded an age of 11843 ± 63 yr BP. Hence, the dated fossils in the study area are generally older than ~12 ka BP, suggesting that they lived under shallow- to mid-shelf conditions (Fig. 13).

5. Discussion

5.1 Activity of the sand waves

Although sand wave migration cannot be estimated with the available data due to the lack of high-resolution repeated bathymetric surveys, several lines of evidence suggest that the sinuous-crested sand waves are active bedforms. First, the direction of the prevailing SW-trending cold bottom current reported from the area (Korea Strait Bottom Cold Water; KSBCW) is consistent with the orientation of the sand waves (Fig. 3). XBT profile further supports a cold water bottom layer as expected with the occurrence of an active KSBCW (Fig. 7B). Second, the geometric properties of sand waves (h vs λ relationship and their h/λ ratio) are similar to those reported from other parts of the world that are considered currently active (Flemming, 1980; Dyer, 1986). Notably, most of the sinuous crested sand-waves plot above the mean h vs λ relationship, and their h/λ ratio is > 0.03 (Fig. 6A–B). A similar activity index was proposed for sand waves in the Barents Sea (King et al., 2014) and the Mozambique Channel (Miramontes et al., 2019).

In contrast to sinuous-crested sand waves, the curvilinear-crested large sand waves lie below the mean h vs λ relationship, and their h/λ ratio is < 0.03, suggesting that these sand waves are either moribund or have not been active for some time (Fig. 6A–B). They could have been relict, initially formed during lower sea levels. Specifically, one would predict that bottom currents would be stronger at low sea levels (~120 m lower than the present day) partly due to the significant narrowing of the Korea Strait. Then, as sea-level rises, they are maintained by much weaker currents. A plausible mechanism for their symmetrical shape would be the assumption that the area in which the curvilinear-crested sand waves are located has not been exposed to a current of the strength that generated the sand waves for some time. As a consequence the crests of the large sand waves became rounded by weak sediment transport, manifested by current ripples and/or small dunes that are superimposed on the large sand waves. Weaker currents mobilize and rework sand, gradually moving it from crests to troughs, thereby reducing the overall height of the large sand waves and transforming them into more

symmetrical forms (Flemming, 2013). Small dunes superimposed on the large sand waves are common features of subaqueous dunes and are generally considered a proxy for active bedforms (Aliotta and Perillo, 1987; Malikides et al., 1988; King et al., 2014). In the study area, the small superimposed dunes are related to the same currents operating on the southwestern part of the canyon. The currents, however, may be weaker here than in the area where the canyon is narrower, possibly due to funneling within the canyon (see below).

5.2 Evidence for a sediment starved setting

Previous regional observations of the seafloor suggest that the outer southeastern continental shelf of Korea, including the area of this investigation, is mostly covered by relict sediments deposited during MIS 2, when sea level was as much as 120 m lower than present (Fig. 13; Koo et al., 2014). The relict sediment intepretation is consistent with the prevalence of sandy and coarser-grained sediments with abundant shells that are not covered by thick deposits of recent hemipelagic origin (Koo et al., 2014). Although this interpretation is in broad agreement with our paleontological data (Table 3), our geochronologic results suggest that relict sediments also correlate with late MIS 3 and early MIS 1 when sea level was about 50 to 80 m below present (Fig. 13).

The extent and timing of relict-sediment reworking remains unclear. Some of the recovered bryozoans are warm-water Pleistocene species (i.e, *Microprina japonica*, Table 3), suggesting reworking, or local inheritance, from a shallower marine environment. However, many of the bryozoans are cold-water organisms that might have lived in the environment of deposition under the influence of bottom currents in modern times or before the last glacial maximum (Table 3). Unlike sea urchins that can live in sandy environments, bryozoans normally live on bedrock or boulders (Emery, 1966); local reworking from a nearby rocky environment is therefore the most likely explanation for these fossils.

The morphology of the sand waves provides additional constraints on low sediment availability in the study area. The h vs λ relationship of the sand waves indicates that they have not reached their critical size (Fig. 6A), which is a feature characteristic of environments with low sediment supply (Flemming, 1980; Dyer, 1986; Miramontes et al., 2019). In addition, the sand waves have gentle to moderate lee-side slopes (< 20 degrees), small heights (< 2 m), and regularly spaced crests (Figs. 3B and 4), which are features observed in flume experiments on supply-limited dunes (e.g., Tuijnder et al., 2009). Moreover, scoured depressions and bedrock exposures in the study area indicate that unconsolidated sediment is being actively removed next to the sand wave field (Fig. 2), consistent with overall limited sediment supply and deposition.

5.3 Possible controls on the formation of the sand waves

The geometry of sinuous-crested sand waves clearly documents the occurrence of unidirectional SW-trending bottom currents in the study area (Figs. 2 and 3). In addition, spatial restriction of sand waves along a submarine canyon suggests a genetic link between the seafloor morphology and sediment accumulation on the sediment-starved Korean shelf. A causal relationship between sand waves and the presence of a narrowing channel or trough has been documented or suggested at other continental margins (e.g., Kubo et al., 2004; Barrie et al., 2009; Lo Iacono et al., 2010; Rovere et al., 2019). Barrie et al. (2009) analyzed multibeam data from the Pacific margin of Canada to show that a confined morphological depression can

enhance current flow, resulting in substrate erosion and provision of sediment for the development of subaqueous dunes. Confined bathymetric restrictions on the Ebro continental shelf also appear to increase the strength of bottom currents, leading to development of very large dunes (Lo Iacono et al., 2010). Similarly, current-generated bedforms were found on a sandy seafloor at water depths of 200–400 m on the northern Izu Ridge, Japan, interpreted to be the product of the Kuroshio Current controlled by local topography (Kubo et al., 2004). Recently Rovere et al. (2019) suggested that muddy sediment waves of the SW Adriatic margin form exclusively within a narrowing shelf, indicating the accelerating effect of the geostrophic currents. Other examples of extensive dune fields where bathymetric control of current flow is pronounced include Bungo Channel, Japan (Ikehara, 1998), Torres Strait off Northern Australia (Harris, 1988), and the mouth of San Francisco Bay (Barnard et al., 2006).

Several mechanisms can lead to the occurrence of unidirectional and bidirectional bottom currents, with significant implications for the geometry and sedimentary characteristics of sand waves. Three main processes may explain sand wave formation in outer continental margin settings: geostrophic currents, bottom ocean currents, and internal waves. The sand wave fields located on the upper continental slope from the Barents Sea are associated with geostrophic currents (King et al., 2014; Bøe et al., 2015). The asymmetric unidirectional bedforms found on the shelf around the Japanese Islands are linked to the strong ocean bottom currents (Ikehara and Kinoshita, 1994; Kido et al., 2004). Current-generated dunes were also found in the deep waters (~200 to 600 m) on the Mozambique Channel, southwest Indian Ocean (Miramontes et al., 2019). Internal waves forming at the interface between water masses (e.g., Breitzke et al., 2017) is another possible cause for the formation of dunes (Reeder et al., 2011; Ribó et al., 2016; Zhang et al., 2019; Miramontes et al., 2020). However, internal waves generally develop on upper continental slopes where pycnoclines with higher density gradients can develop (Reeder et al., 2011, Ma et al., 2016; Miramontes et al., 2021). This is dissimilar to the deeper marine setting of our study area, where the transition between water masses of distinct densities is yet to be documented. In addition, sand waves influenced by internal waves commonly display diverging migration directions (Ma et al., 2016; Zhang et al., 2019), contrasting with the patterns of sinuous-crested sand waves observed in the upper part of the studied canyon. Therefore, we conclude that the most likely mechanism to account for the formation of the sinuous-crested asymmetrical sand waves is bottom currents related to the SW-trending KSBCW that has been documented regionally (Shin et al., 2006). In contrast, the symmetrical bedforms in the deeper part of the study area suggest they are either moribund or have not been active for some time.

Our MBES data reveal that the sand waves are increasing in height towards the SW, where the studied canyon gets narrower and and sand wave geometry transitions from symmetrical to asymmetrical (Figs. 2 and 4). As suggested for other shelf environments (e.g., Kubo et al., 2004; Barrie et al., 2009), this observation is best explained by the strengthening of bottom currents in response to topographically-induced funneling. In addition, several studies have previously documented a positive correlation between bedform size and current velocity in shallow estuary and relatively deep marine settings. For instance, Rubin and McCulloch (1980) found a good correlation between dune height and current velocity in San Francisco Bay. McCave (1971), studying the dunes in the North Sea, also observed a good correlation between current velocity and dune height. Further support in favor of high energy bottom currents in the study area comes from recent current estimates of the KSBCW based on Acoustic Doppler Current Profiler (ADCP) data that suggests current velocities of 25 cm/s at depths > 150 m (Shin et al., 2006). Strengthening of bottom currents towards the SW could

also provide an explanation for the preservation of symmetrical curvilinear-crested sand waves in the NE entrance of the canyon. In this area, bottom currents might never be strong enough to mobilize sandy and coarser sediments, and bedforms might inherit their geometry.

Our samples provide additional support for the strengthening of bottom currents toward the SW of the sand wave field. Sediment grain size and sorting are commonly correlated with the size of sand waves (McCave 1971; Flemming, 1978, 2000; Dalrymple et al., 1978; Rubin and McCulloch, 1980; Bartholdy et al., 2002; Francken et al., 2004; Van Landegman et al., 2012). Dalrymple et al. (1978), in an analysis of bedforms in the Bay of Fundy, observed that the largest bedforms occur in coarser sands. Similarly, Rubin and McCulloch (1980) and Bartholdy et al. (2002) found a distinct relationship between grain size and dune height in San Francisco Bay and the Danish Wadden Sea, respectively. Wilcock (1992) and Van Oyen and Blondeaux (2009) further reported that the size and shape of sandy bedforms might depend not only on grain size but also on sediment sorting. In accord with these studies, our results show a good correlation between grain size/sorting and sand wave height; typically, larger amplitude sand waves tend to have better sorted and coarser sediments (i.e., P10 and P11; Figs. 4A-10A). Good sorting is probably related to the steadiness of the flow velocity at the time scale of active sediment transport, while the grain size correlates to the maximum flow velocity (Rubin and McCulloch, 1980). Using these simple criteria, granulometric properties in sinuous-crested sand waves appear consistent with the funneling of relatively steady currents in the canyon, with an increase in the flow strength from P13 to P11 and P10 (Fig. 10B). Towards the exit of the sand wave area, bathymetric features projecting above the seafloor might cause turbulence or rapid fluctuations in the current, ultimately resulting in a decrease of sediment sorting towards P10 (Fig. 10B). Turbulences or eddies are commonly formed around obstacles on the seafloor and can create erosion or prevent sediment deposition (e.g., Rebesco et al., 2014; Wilckens et al., 2021). Similarly, the bathymetric depressions towards the SW of the study area, near the SW edge of the sand waves field, suggest erosion by eddies (Fig. 2); this is consistent with the strengthening of the current within the canyon due to funneling effects.

5.4 Flow velocity estimation of the observed sand waves

We estimated flow velocities for initiation and growth of the sinuous-crested sand waves by substituting Eqs. (1) and (3) into Eq. (2) (see section 3). The estimated flow velocities for water depths of 180 m to 190 m covering the sand wave field are in the range of 3.68 m/s and 3.87 m/s (for a grain size of 0.38 mm and 0.45 mm, respectively) for the initial stage of bedform development (assuming a flat seafloor). These velocities are remarkably higher than the measured velocities (ca. 0.25 m/s) for the southwestward flowing bottom current (KSBCW) observed in a nearby area (See ADCP line in figure 1; Shin et al., 2006). Once sand waves are present and the beds are no longer flat, the roughness would depend more on bedform dimension than the grain size (Kubo et al., 2004). Hence, by using Eq. (4) instead of Eq (3), the surface flow velocity is estimated to be 1.2 m/s and 1.3 m/s (for grain sizes of 0.38 mm and 0.45 mm, respectively) for the largest sand waves with H=2.1 m, L=40 m, and z=180 m. These velocities are closer to the modern oceanographic conditions but still significantly higher than the observed velocity of Shin et al. (2006). However, the ADCP line acquired by Shin et al. (2006) is about 60 km away from our study area in an inner shelf not affected by a rough topography. As discussed above, the flow velocities might be higher in our study area as the KSBCW is expected to accelerate and become constricted up-canyon. The estimated velocity, based on the roughness of wavy beds, is thus interpreted as the necessary velocity to maintain the existing beds. However, long-term current velocity measurements are required to determine

better estimates in our study area.

5.5 Sedimentary evidence for fluctuating sand wave migration

As discussed above, bathymetric and core data from the study area document two types of sand waves: (1) sinuous-crested asymmetrical sand waves associated with on-going, upslope transport by bottom currents within a channel, and (2) curvilinear-crested symmetrical sand waves possibly formed by an older strong bottom current, followed by minor reworking by modern bottom currents. The nature and age of the material found in the sand waves is in agreement with previous regional studies and indicate a relatively limited supply of sand within a sediment-starved shelf environment (Koo et al., 2014; Chun et al., 1999). The post-glacial sea-level changes in the study area may have affected the mode and rate of sediment transport in the sand wave field at millennial to multi-millennial time scales. However, granulometric and compositional characteristics of the sand within the cores are overall similar, indicating that the maximum flow velocity associated with the transport of the sand remained fairly similar during the formation of the observed sand waves.

Additional constraints on bedform formation and dynamics in the study area come from our detailed sand analysis, which reveals a ubiquitous decrease in the grain size and sorting in the topmost ~20 cm of the 4 retrieved piston cores (Fig. 10B). These changes are well correlated with a systematic increase in the carbonate content of the sand, which supports the existence of a fine, carbonate-rich fraction at the top of the cores (e.g., topmost sample in core P10 in Fig. 11). Core microscope observations indicate that this fraction is composed of plankton and carbonate silt, which represents a pelagic component that is absent or significantly less abundant in the lower (older) sand deposits. A simple explanation that can account for these granulometric and compositional changes is that fine and possibly lower density pelagic deposits are only preserved transiently at the top of the sand waves and are periodically removed by winnowing during periods of bottom current strengthening. Although numerical modeling suggests that ripples superimposed on dunes can spontaneously develop in well-sorted sand transported by steady currents (e.g., Vinent et al., 2019), the changes in grain size observed in the study area require additional variability in the system, such as a fluctuating flow regime. Therefore, similar to observations in some other well-documented sand wave fields (e.g., Van Oyen and Blondeaux, 2009), our sand analysis strongly suggests that the migration of the studied sand waves occurs only episodically due to an inherently fluctuating intensity of bottom currents on the southeastern continental Korean shelf. Although this interpretation remains to be confirmed by repeated imaging of the study area to document the rate and frequency of sand wave migration, our results show that characterizing the sedimentary nature of sand deposits can offer a valuable insight into possibly fluctuating hydrodynamic conditions on the seafloor.

6. Conclusions

(1) We document > 110 sinuous- and curvilinear-crested sand waves in water depths of 180–190 within a gentle shelf-incised canyon on the southeastern continental shelf of Korea. The sinuous-crested bedforms are asymmetric and have wavelengths of 10 to 45 m and amplitudes of up to 2.1 m. The large curvilinear-crested sand waves in the lower part of the canyon are symmetrical with an average wavelength of ~100 m and an average wave height of ~ 2 m.

(2) Sand wave geometry suggests upslope sediment transport direction, consistent with the occurrence of the SW-directed Korea Strait Bottom Cold Water Current in the study area. Sand-wave occurrence within the canyon suggests bottom currents accelerated due to the funnelling effects of the shelf-incised canyon.

(3) The sinuous- and curvilinear- crested sand waves predominantly consist of a mixture of medium-grained siliciclastic sediments. Granulometric and compositional characteristics of the sediment indicate fluctuating hydrodynamic conditions and episodic sand wave mobility. They are commonly capped by more fine-grained carbonate deposits rich in plankton, suggesting pelagic deposition.

(4) Radiocarbon and palaeontological data indicate that the macrofossils formed in shallow-marine conditions at times of lower sea level, MIS 3 and early MIS 1. They were subsequently transported to the canyon-incised outer shelf setting that is presently sediment starved. Bottom current velocities, sediment transport, and sand-wave formation are inferred to have been significantly influenced by post-glacial sea level changes.

(5) Overall, our study provides an important example of sand waves in an outer shelf sediment-starved environment. It shows that a granulometric and compositional sediment analysis coupled with radiocarbon dating of fossils can constrain transient geological and hydrodynamic processes associated with the formation of sand waves, from multi-millennial to contemporaneous time scales.

Data availability

The data used in this paper are classified but can be shared through cooperative projects after 3 years of moratorium period.

Declaration of Competing Interest

The authors in this paper declare no conflicts of interests.

Acknowledgments

This work was supported by the “Development of the integrated geophysical survey and real-scale data processing technologies for 3D high-resolution imaging of the marine subsurface” project (research fund number: 21–3312-1) of the Korea Institute of Geoscience and Mineral Resources (KIGAM), South Korea. We thank Dr. Samuel Y. Johnson and three anonymous reviewers for their constructive comments, which led to significant improvements in the original manuscript. We thank the captains, officers, crew and scientific parties of the *RV Tamhae II* for help in data collection.

References

Albarracín, S., Alcántara, J., Montoya, I., Fontán, A., Somoza, L., Amos, C.L., Rey, J., 2014. Relict Sand Waves in the Continental Shelf of the Gulf of Valencia (Western Mediterranean). J. Sea Res. 93, 33–46.

Aliotta, S., Perillo, G.M.E., 1987. A sand wave field in the entrance to Bahia Blanca Estuary,

Argentina. Mar. Geol. 76, 1–14.

Allen, J.R.L., 1972. Instability of an upper-phase plane bed: a test of Bagnold's criterion. Sediment Geol. 8, 309–316.

Allen, P.A., Homewood, P., 1984. Evolution and mechanics of a Miocene tidal sandwave. Sedimentology 31,63–81.

Ashley, G.M., 1990. Classification of large-scale subaqueous bedforms: a new look at an old problem. SEPM Bedforms and Bedding Structure Research Symposium. J. Sed. Geol. 60 (1), 160–172.

Barnard, P.L., Hanes, D.M., Rubin, D.M., Kvitek, R.G., 2006. Giant sand waves at the mouth of San Francisco Bay. Eos 87 (29), 285–289.

Barrie, J.V., Conway, K.W., Picard, K., Greene, H.G., 2009. Large-scale sedimentary bedforms and sediment dynamics on a glaciated tectonic continental shelf: examples from the Pacific margin of Canada. Cont. Shelf Res. 29 (5–6), 796–806.

Bartholdy, J., Bartholomae, A., Flemming, B.W., 2002. Grain-size control of large compound flow-transverse bedforms in a tidal inlet of the Danish Wadden Sea. Mar. Geol. 188, 391–413.

Belde, J., Reuning, L., Back, S., 2017. Bottom currents and sediment waves on a shallow carbonate shelf, Northern Carnarvon Basin, Australia. Cont. Shelf Res. 138, 142–153.

Breitzke, M., Wiles, E., Krocker, R., Watkeys, M.K., Jokat, W., 2017. Seafloor morphology in the Mozambique Channel: evidence for long-term persistent bottom-current flow and deep-reaching eddy activity. Mar. Geophys. Res. 38, 241–269.

Bøe, R., Bellec, V.K., Dolan, M.F.J., Buhl-Mortensen, P., Buhl-Mortensen, L., Slagstad, D., Rise, L., 2009. Giant sandwaves in the Hola glacial trough off Vesterålen, North Norway. Mar. Geol. 267, 36–54.

Bøe, R., Skarðhamar, J., Rise, L., Dolan, M.F.J., Bellec, V.K., Winsborrow, M., Skagseth, Ø., Knies, J., King, E.L., Walderhaug, O., Chang, S., Buenz, S., Miniert, J., 2015. Sandwaves and sand transport on the Barents Sea continental slope offshore northern Norway. Mar. Pet. Geol. 60, 34–53.

Chang, K.-I., Teague, W.J., Lyu, S.J., Perkins, H.T., Lee, D.-K., Watts, D. R., Kim, Y.-B., Mitchell, D. A., Lee, C.M., Kim, K., 2004. Circulation and currents in the southwestern East/Japan Sea: Overview and review. Prog. Oceanogr. 61,105–156.

Chappel, J., Shackleton, N.J., 1986. Oxygen isotopes and sea level. Nature 324, 137–140.

Cho, Y.K., Kim, K., 1998. Structure of the Korea Strait Bottom Cold Water and its seasonal variation in 1991. Cont. Shelf Res. 18(7), 791–804.

Cho, Y.K., Kim, K., 1999. Branching mechanism of the Tsushima Current in the Korea Strait. J. Phys. Oceanogr. 30(11), 2788–2797.

Choi, K.S., Cha, Y.M., Kim, T.R., 2012. Decadal change of frequency in Korea landfalling tropical cyclone activity (in Korean with English abstract). J. Korea Earth Sci. Soc. 33, 49–58.

Chun, J.H., Huh, S., Han, S.J., Shin, D.H., Cheong, D.K., Hong, K.H., Kim, S.H., 1999.

Sediment characteristics of waste disposal sites in the southwestern Ulleung Basin, the East Sea. J. Korean Soc. Oceanog. 4, 312–322.

Chun, J.H., Kim, Y., Bahk, J.J., Kim, Y.J., Kang, D.H., Kim, G.Y., Ryu, B.J., 2015. Late Holocene distal mud deposits off the Nakdong delta, SE Korea: evidence for shore-parallel sediment transport in a current-dominated setting. Geo-Mar. Lett. 35, 475–485.

Dalrymple, R.W., Knight, J.R., Lambiase, J.J., 1978. Bedforms and their hydraulic stability relationships in a tidal environment, Bay of Fundy, Canada. Nature 275, 100–104.

Dalrymple, R.W., LeGresley, E.M., Fader, G.B.J., Petrie, B.D., 1992. The western Grand Banks of Newfoundland: transgressive Holocene sedimentation under the combined influence of waves and currents. Mar. Geol. 105 (1–4), 95–118.

Droghei, R., Falcini, F., Casalbore, D., Martorelli, E., Mosetti, R., Sannino, G., Santoreli, R., Chiocci, F.L., 2016. The role of Internal Solitary Waves on deep-water sedimentary processes: the case of up-slope migrating sediment waves off the Messina Strait. Sci. Rep. 6, 36376.

Dyer, K.R., 1986. Coastal and Estuarine Sediment Dynamics. John Wiley & Sons, Chichester, 342 p.

Emery, K., 1966. The Atlantic Continental Shelf and Slope of the United States-geologic background. U.S. Geol. Survey Professional Paper 529-A, 23 p.

Ernstsen, V.B., Noormets, R., Hebbeln, D., Bartholoma, A., and Flemming, B.W., 2006, Precision of high-resolution multibeam echo sounding coupled with high-accuracy positioning in a shallow water coastal environment. Geo-Mar. Lett. 26, 141–149.

Flemming, B.W., 1978. Underwater sand dunes along the southeast African continental margin-observations and implications. Mar. Geol., 26, 177–198.

Flemming, B.W., 1980. Sand transport and bedform patterns on the continental shelf between Durban and Port Elizabeth (southeastern African continental margin). Sediment. Geol. 26, 179–205.

Flemming, B.W.,1988. Zur klassifikation subaquatischer, strömungstransversaler transportkörper. Bochumer Geol. Geotech. Arb. 29, 44–47.

Flemming, B.W., 2000. The role of grain size, water depth and flow velocity as scaling factors controlling the size of subaqueous dunes. In: Trentesaux, A., Garlan, T., (Eds.), Proceedings of the First International Workshop on Marine Sandwave Dynamics, Univ. of Lille, Lille, France, pp. 55–60.

Flemming, B.W., 2013. Comment on “large-scale bedforms along a tideless outer shelf setting in the western Mediterranean” by lo Iacono et al. (2010) in continental shelf research vol 30, pp 1802–1813. Cont. Shelf Res. 52, 203–207.

Folk, R.L., Ward, W.C., 1957. Brazos River Bar—a study in the significance of grain size parameters. Jour. Seal. Petrology 27, 3–26.

Francken, F., Wartel, S., Parker, R., Taverniers, E., 2004. Factors influencing subaqueous dunes in the Scheldt Estuary. Geo-Mar. Lett. 24, 14–21.

Harris, P.T., 1988. Sediments, bedforms and bedload transport pathways on the continental shelf adjacent to Torres Strait, Australia-Papua New Guinea. Cont. Shelf Res. 8, 979–

1003.

Hernández-Molina F.J., Campbell, S., Badalini, G., Thompson, P., Walker, R., Soto, M., Conti, B., Preu, B., Thieblemont, A., Hyslop, L., Miramontes, E., Morales, E., 2017. Large bedforms on contourite terraces: sedimentary and conceptual implications. Geology 46, 27–30.

Horozal, S., Chae, S., Seo, J.M., Lee, S.M., Han, H.S., Cukur, D., Kim, E.D., Son, J.H., 2021. Quaternary evolution of the southeastern Korean continental shelf, East Sea: Paleo-incised valley and channel systems. Mar. Pet. Geol. 128, 105011.

Ikehara, H., Kinoshita, Y., 1994. Distribution and origin of subaqueous dunes on the shelf of Japan. Mar. Geol. 120 (1-2), 75–87.

Ikehara, K., 1998. Sequence stratigraphy of tidal sand bodies in the Bungo Channel, southwest Japan. Sediment. Geol. 122, 233–244.

ITTC Recommended Procedures, 2011. Fresh Water and Seawater Properties. Report 7.5-02-01-03, Pages 1 of 45.

Julien, P.Y., 1998. Erosion and sedimentation. Cambridge University Press, Cambridge.

Kim, Y.H., Kim, Y.B., Kim, K., Chang, K.I., Lyu, S.J., Cho, Y.K., Teague, W.J. 2006. Seasonal variation of the Korea Strait Bottom Cold Water and its relation to the bottom currents. Geophy. Res. Lett. 33, L24604.

King, E.L., Bøe, R., Bellec, V.K., Rise, L., Skarðhamar, J., Ferre, B., Dolan, M., 2014. Contour current driven continental slope-situated sandwaves with effects from secondary current processes on the Barents Sea margin offshore Norway. Mar. Geol. 353, 108–127.

Knebel, H. J., Folger, D.W.,1976. Large sand waves on the Atlantic Outer Continental Shelf around Wilmington Canyon, off Eastern United States. Mar. Geol. 22 (1), 7–15.

Koo, B.Y., Kim, S.P., Lee, G.S., Chung, G.S., 2014. Seafloor morphology and surface sediment distribution of the southwestern part of the Ulleung Basin, East Sea. J. Korean Sci. Soc. 35(2), 131–146.

Kubo, Y., Soh, W., Machiyama, H., Tokuyama, H., 2004. Bedforms produced by the Kuroshio Current passing over the northern Izu Ridge.Geo. Mar. Lett. 24(1), 1–7.

Lee, J.C., Kim, D.H., 2016. Observations of Bottom Currents in the Korea Strait. Korean J. Fish. Aquat. Sci. 49, 393-403.

Lo Iacono, C., Guillen, J., Puig, P., Ribo, M., Ballesteros, M., Palanques, A., li Farran, M., Acosta, J., 2010. Large-scale bedforms along a tideless outer shelf setting in the western Mediterranean. Con. Shelf Res. 30, 1802–1813.

Lo Iacono, C., Guillén, J., Guerrero, Q., Durán, R., Wardell, C., Hall, R. A., Aslam, T., Carter, G.D.O., Gales, J.A., Huvenne, V.A.I., 2020. Bidirectional bedform fields at the head of a submarine canyon (NE Atlantic). Earth Planet. Sci. Lett. 542, 116321.

Ma, X., Yan, J., Hou, Y., Lin, F., Zheng, X., 2016.Footprints of obliquely incident internal solitary waves and internal tides near the shelf break in the northern South China Sea. J. Geophys. Res. Oceans 121 (2016), 8706–8719.

Ma, X.C., Yan, J., Song, Y.D., Liu, X.S., Zhang, J.X., Traykovski, P.A., 2019. Morphology and

maintenance of steep dunes near dune asymmetry transitional areas on the shallow shelf (Beibu Gulf, northwest South China Sea). Mar. Geol. 412, 37–52.

Malikides, M., Harris, P. T., Jenkins, C. J. and Keene, J. B., 1988. Carbonate sandwaves in Bass Strait. Austral. J. Earth Sci. 35, 303–311.

McCave, I.N., 1971. Sand waves in the North Sea off the coast of Holland. Mar. Geol. 10, 199–225.

Min, H.S., Kim, Y.-H., Kim, C.-H., 2006. Year-to-year variation of cold waters around the Korea Strait. Ocean Sci. J. 41 (4), 227–234.

Miramontes, E., Jouet, G., Thereau, E., Bruno, M., Penven, P., Guerin, C., Le Roy, P., Deoz, L., Jorry, S.J., Hernandez-Molina, F.J., Thieblemont, A., Jacinto, R.S., Cattaneo, A., 2020. The impact of interna l waves on upper continental slopes: insights from the Mozambican margin (southwest Indian Ocean). Earth Surf. Process. Landforms 45, 1469–1482.

Miramontes, E., Penven, P., Fierens, R., Droz, L., Toucanne, S., Jorry, S.J., Jouet, G., Pastor, L., Silva Jacinto, R., Gaillot, A., Giraudeau, J., Raisson, F., 2019. The influence of bottom currents on the Zambezi Valley morphology (Mozambique Channel, SW Indian Ocean): in situ current observations and hydrodynamic modelling. Mar. Geol. 410, 42–55.

Miramontes, E., Thieblemont, A., Babonneau, N., Penven, P., Raisson, F., Droz, L., Jorry, S.J., Fierens, R., Counts, J.W., Wilckens, H., 2021. Contourite and mixed turbidite-contourite systems in the Mozambique Channel (SW Indian Ocean): Link between geometry, sediment characteristics and modelled bottom currents. Mar. Geol. 437, 106502.

Na, H., Kim, K.Y., Chang, K.I., Kim, K., Yun, J.Y., Minobe, S., 2010. Interannual variability of the Korea Strait Bottom Cold Water and its relationship with the upper water temperatures and atmospheric forcing in the Sea of Japan (East Sea). J. Geophys. Res. 115(C09031), 1–11.

Nemeth, A.A., Hulscher, S.J.M.H., de Vriend, H.J., 2002. Modelling sand wave migration in shallow shelf areas. Cont. Shelf Re. 22(18-19), 2795–2806.

Normandeau, A., Lajeunessa, P., St-Onge, G., Bourgault, D., Droun, S.O., Senneville, S., Belanger, S., 2014. Morphodynamics in sediment-starved inner-shelf submarine canyons (Lower St. Lawrence Estuary, Eastern Canada. Mar. Geol. 357, 243–255.

Park, S.C., Hong, S.K., Kim, D.C., 1996. Evolution of late quaternary deposits on the innershelf of the south sea of Korea. Mar. Geol. 131, 219–232.

Park, S.C., Yoo, D.G., Lee, C.W., Lee, E.L., 2000. Last glacial sea-level changes and paleogeography of the Korea (Tsushima) Strait. Geo-Mar. Lett. 20, 64–71.

Park, Y.G., Cho, Y.K., Kim, K., 1995. A hydraulic model of the Korea Strait bottom cold current. J. Oceanogr. 51, 719–727.

Rebesco, M., Hernández-Molina, F. J., Van Rooij, D., Wåhlin, A., 2014. Contourites and associated sediments controlled by deep-water circulation processes: State-of-the-art and future considerations. Mar. Geol. 352, 111–154.

Reeder, D.B., Barry, B.M., Yang, Y.J., 2011. Very large subaqueous sand dunes on the upper

continental slope in the South China Sea generated by episodic, shoaling deep- water internal solitary waves. Mar. Geol. 279, 12–18.

Ribó, M., Puig, P., Muñoz, A., Lo Iacono, C., Masqué, P., Palanques, A., Acosta, J., Guillén, J., Gómez Ballesteros M., 2016. Morphobathymetric analysis of the large fine-grained sediment waves over the Gulf of Valencia continental slope (NW Mediterranean). Geomorphology 253, 22–37.

Rovere, M., Pellegrini, C., Chiggiato, J., Campiani, E., Trincardi, F., 2019. Impact of dense bottom water on a continental shelf: An example from the SW Adriatic margin. Mar. Geol. 408, 123–143.

Rubin, D.M., McCulloch, D.S., 1980. Single and superimposed bedforms: A synthesis of San Francisco Bay and flume observations. Sediment. Geol., 26, 207–231.

Shin, C.W., Kim, C., Byun, S.K., Jeon, D., Hwang, S.C., 2006. Southeastward intrusion of Korea Strait Bottom Cold Water observed in 2003 and 2004. Ocean Sci. J. 41 (4), 291–299.

Stanford, J.D., Hemingway, R., Rohling, E.J., Challenor, P.G., Medina-Elizalde, M., and Lester, A.J., 2011, Sea-level probability for the last deglaciation—A statistical analysis of far-field records. Glob. Planet. Change 79, 193–203.

Stow, D.A.W., Hernández-Molina, F. J., Llave, E., Sayago-Gil, M., Díaz del Río, V., Branson, A., 2009. Bedform-velocity matrix: The estimation of bottom current velocity from bedform observations. Geology 37 (4), 327–330.

Takikawa, T., Yoon, J. H., Cho, K.D., 2005. The Tsushima warm current through Tsushima Straits estimated from ferryboat ADCP data. J. Phys. Oceanogr. 35(6), 1154–1168.

Teague, W.J., Perkins, H.T., Jacobs, G.A., Book, J.W., 2001. Tide observations in the Korea-Tsushima Strait. Cont. Shelf Res. 21(5), 545–561.

Teague, W.J., Ko, D.S., Jacobs, G.A., Perkins, H.T., Book, J.W., Smith, S.R., Chang, K.I., Suk, M.S., Kuh, K., Lyu, S.J., Tang, T.Y., 2006. Currents through the Korea/Tsushima Strait: A review of LINKS observations. Oceanography 19, 50–63

Tuijnder, A.P., Ribberink, J.S., Hulscher, S.J.M.H., 2009. An experimental study into the geometry of supply-limited dunes. Sedimentology 56, 1713–1727.

Van Landeghem, K.J.J., Bass, J.H., Mitchell, N.C., Wilcockson, D., Wheeler, A.J., 2012. Reversed sediment wave migration in the Irish Sea, NW Europe: A reappraisal of the validity of geometry-based predictive modelling and assumptions. Mar. Geol. 295, 95–112.

Van Landeghem, K.J.J., Wheeler, A.J., Mitchell, N.C., Sutton, G., 2009. Variations in sediment wave dimensions across the tidally dominated Irish Sea, NW Europe. Mar. Geol. 263, 108–119.

Van Oyen, T., Blondeaux, P., 2009. Grain sorting effects on the formation of tidal sand waves. J. Fluid Mech. 629, 311–342.

Viana, A.R., Faugeres, J.C., Stow, D.A.V., 1998. Bottom-current-controlled sand deposits a review of modem shallow- to deep-water environments. Sed. Geol. 115, 53–80.

Vinent, D.O., Andreotti, B., Claudin, P., Winter, C., 2019. A unified model of ripples and dunes

in water and planetary environments. Nature Geosci. 12, 345–350.

Waelbroeck, C., Labeyrie, L., Michel, E., Duplessy, J.C., McManus, J.F., Lambeck, K., Balbon, E., and Labracherie, M., 2002. Sea-level and deep water temperature changes derived from benthic foraminifera isotopic records. Quat. Sci. Rev. 21, 295–305.

Wilckens, H., Miramontes, E., Schwenk, T., Artana, C., Zhang, W., Piola, A.R., Baques, M., Provost, C., Hernández-Molina, F. J., Felgendreher, M., Spieß, V., Kasten, S., 2021.The erosive power of the Malvinas Current: Influence of bottom currents on morpho-sedimentary features along the northern Argentine margin (SW Atlantic Ocean). Mar. Geol. 439, 106539.

Wilcock, P.R., 1992. Experimental investigation of the effect of mixture properties on transport dynamics. In: Billi, P., Hey, R.D., Thorne, C.R., Tacconi, P. (Eds.), Dynamics of gravel-bed rivers. Wiley, Chichester, pp 109–131.

Wooding, R.A., Bradley, E.F., Marshall, J.K., 1973. Drag due to regular arrays of roughness elements of varying geometry. Boundary Layer Meteorol. 5, 285–308.

Wynn, R.B., Stow, D.A., 2002. Classification and characterization of deep-water sediment waves. Mar. Geol. 192, 7–22.

Ye Yincan et al., 2017. Chapter 12-Submarine sand waves and sand ridges. In: Ye Yincan et al. (Eds.), Marine geo-hazards in China, Elsevier, pp. 523–554.

Yun, J.-Y., Magaard, L., Kim, K., Shin, C.-W., Kim, C., Byun, S.-K., 2004. Spatial and temporal variability of the North Korean Cold Water leading to the near bottom cold water intrusion in Korea Strait. Progr. Oceanogr. 60, 99–131.

Zhang, H., Ma, X., Zhuang, L., Yan, J., 2019. Sand waves near the shelf break of the northern South China Sea: morphology and recent mobility. Geo-Mar. Lett. 39, 19–36.

Zhou, J., Wu, Z., Zhao, D., Guan, W., Zhu, C., Flemming, B.W., 2020. Giant sand waves on the Taiwan Banks, southern Taiwan Strait: Distribution, morphometric relationships, and hydrologic influence factors in a tide-dominated environment. Mar. Geol. 427(3), 106238.

FIGURES

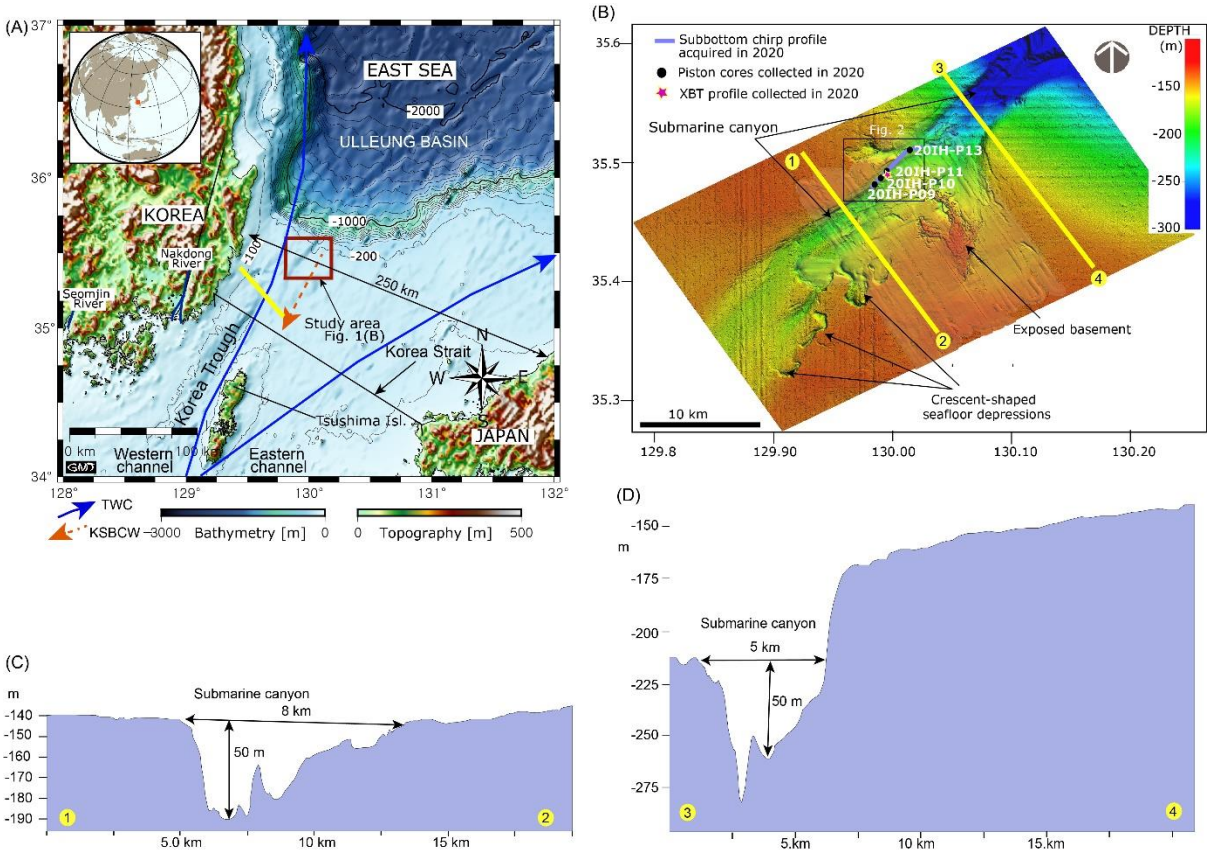

Fig. 1: (A) Bathymetry of the southeastern continental shelf of the Korean Peninsula and adjoining areas. TWW and KSBCW denote the Tsushima Warm Current and the Korea Strait Bottom Cold Water (adopted from Cho and Kim, 2000). Thick yellow line represents ADCP (acoustic Doppler current profiler) line adopted from Shin et al. (2006). The study area shown in figure 2 is marked with a red box. **(B)** Hillshaded multibeam echosounder (MBES) data with sun illumination from NNE showing the location of the study area and the sub-bottom chirp profile, XBT profile, and piston cores. The MBES data also show numerous crescent-shaped seafloor depressions, exposed basement, and a submarine canyon head in which our study area is located. Water depths on the outer shelf range from less than 130 m to over 220 m. (C), (D) Bathymetric profiles across the shelf-incised canyon, revealing widths and heights of up to 8 km and 50 m, respectively.

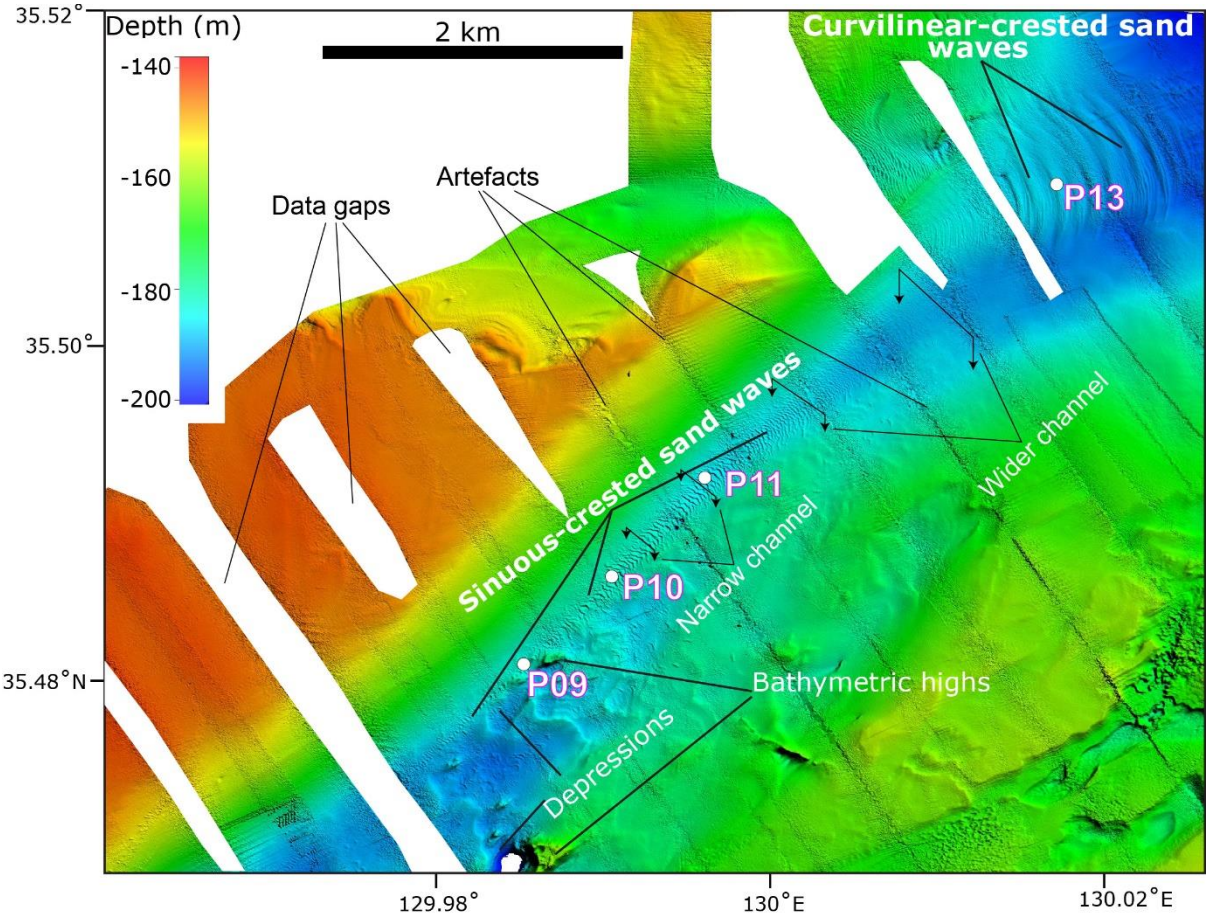

Fig. 2: Multibeam-based bathymetry of the study area showing the axis of the present-day submarine canyon floor that contains numerous NW-SE-trending sinuous-crested sand waves in water depths of 180-190 m. Note that the amplitude of sand waves increases towards the SW, where the channel gets narrow and then decreases to the SW exit of the sand wave field. Large curvilinear-crested sand waves occur in the NE corner of the study area.

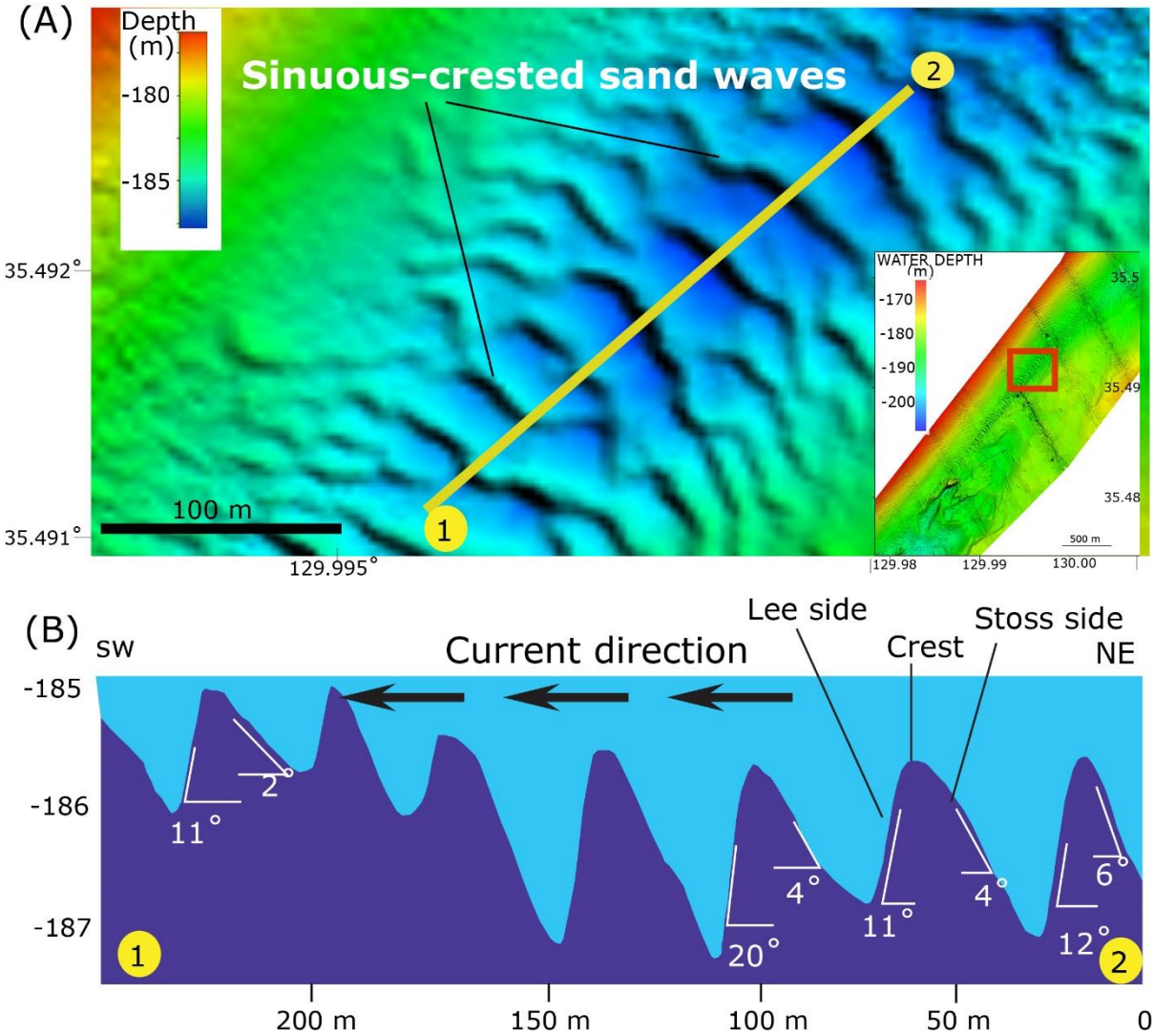

Fig. 3: (A) Bathymetric data showing NW-SE-trending sinuous-crested sand waves. **(B)** Bathymetric profile showing their asymmetry and heights up to 2 m with lee side slopes of 11-20°. The asymmetrical morphology indicates that currents flow towards the SW.

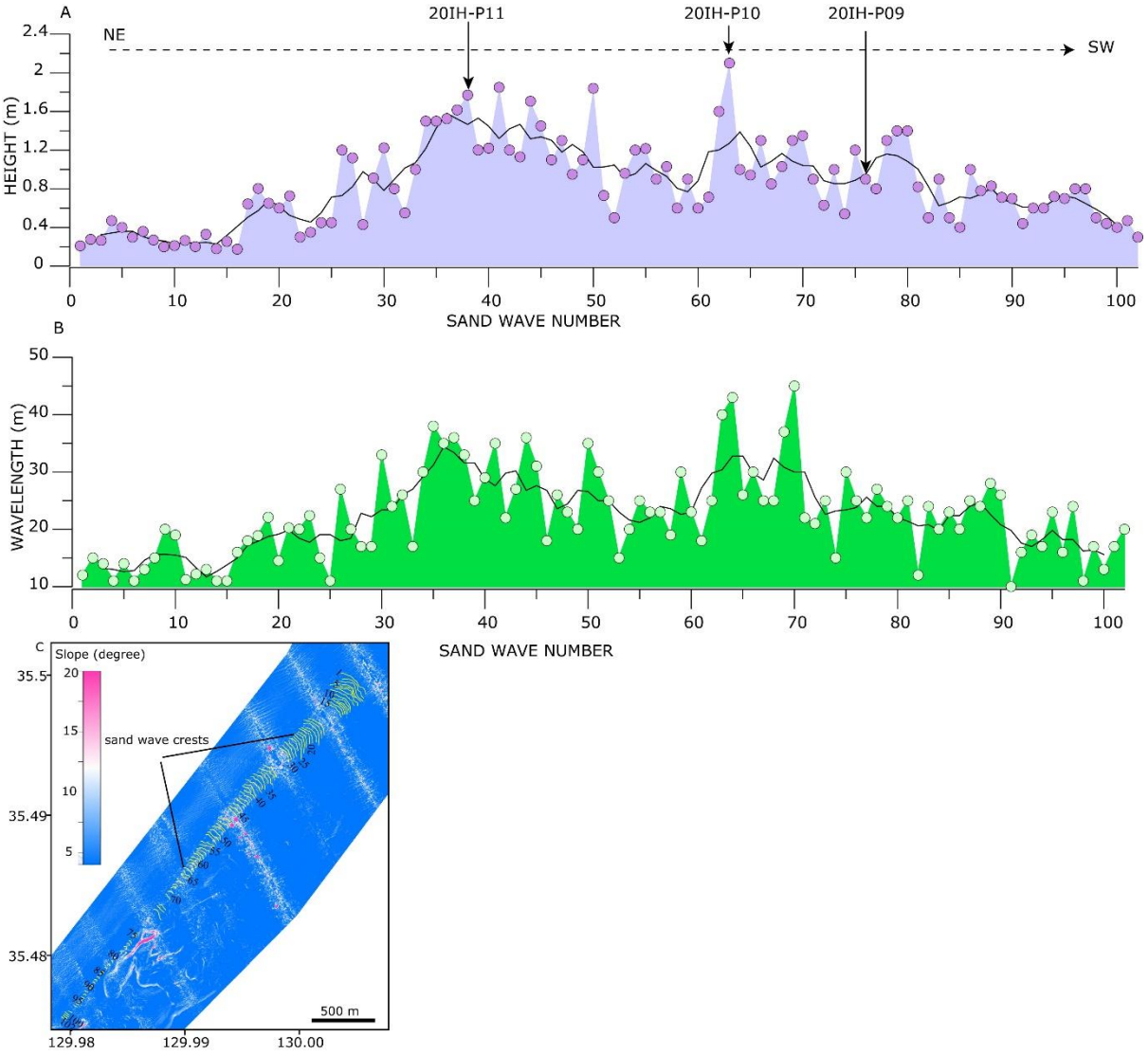

Fig. 4: (A) Height and **(B)** wavelength versus sand wave numbers observed in the study area. The sand waves are 0.3–2.1 m high, with an average of 1 m. Wavelengths range from 10–45 m, with a mean value of ~24 m. They become higher and wider towards the southwest; their amplitude decreasing again towards the SW end of the sand wave field.

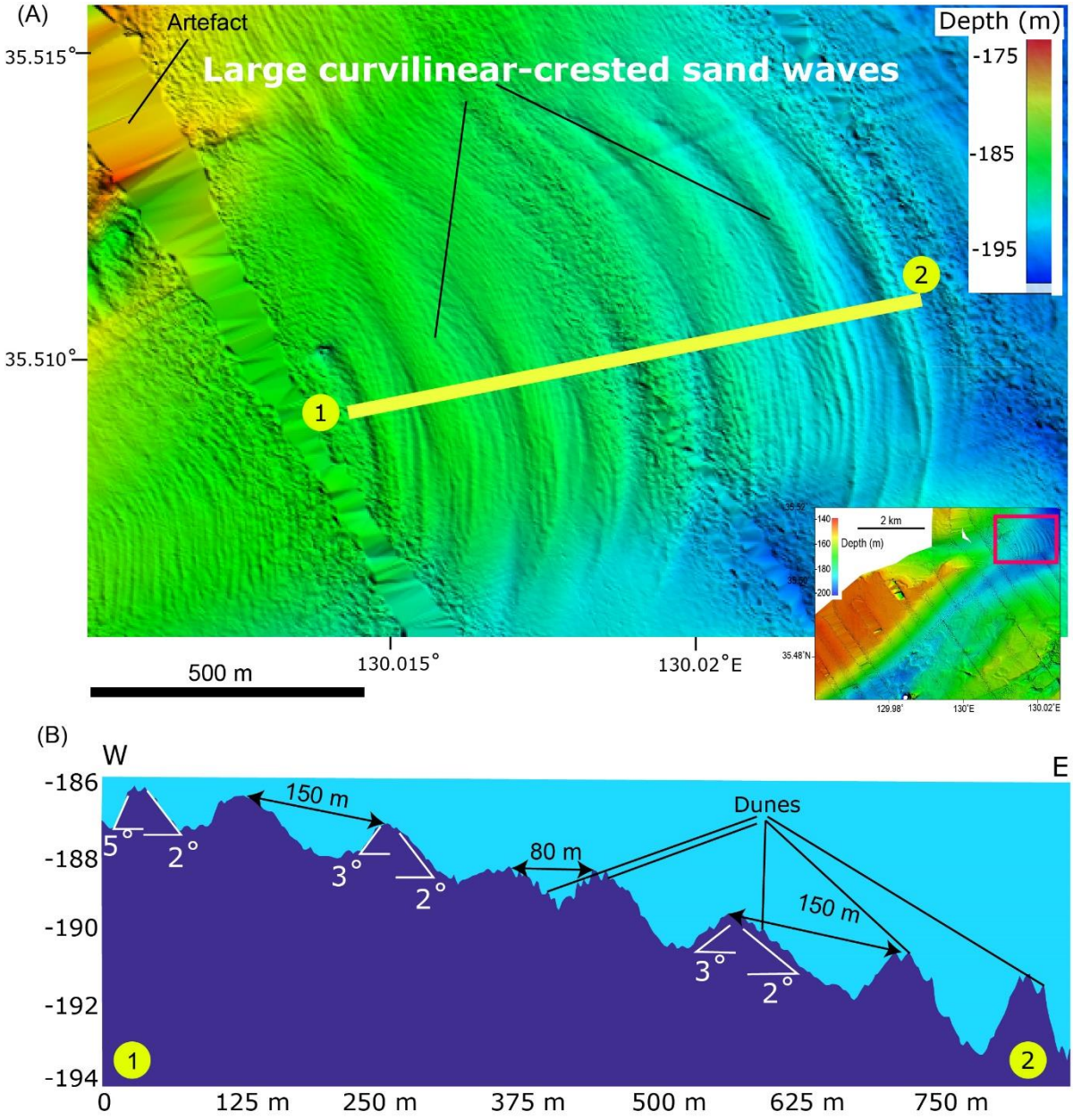

Fig. 5: (A) Multibeam bathymetric data showing NNW-trending curvilinear-crested sand waves. **(B)** Bathymetric profile across the sand waves, which range in width from < 40 m to 80 > with a maximum relief of about 3 m. Also shown are smaller, superimposed dunes on the stoss and lee sides of the larger sand waves.

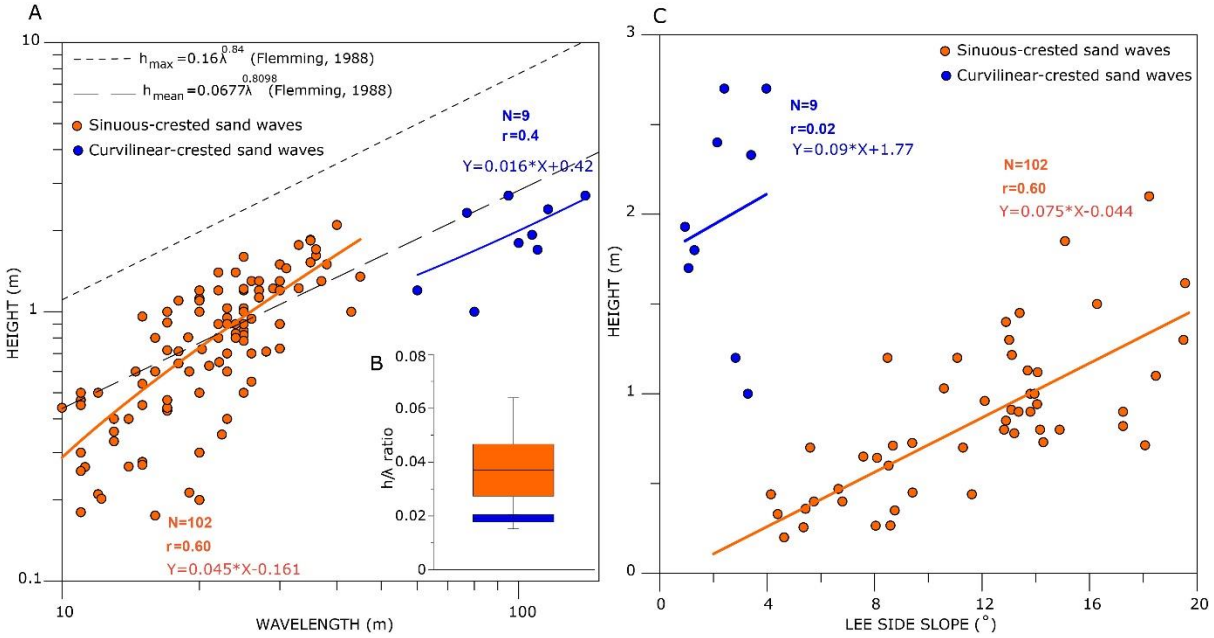

Fig. 6: Height versus wavelength plot for sinuous-crested sand waves (orange color) and curvilinear sand waves (blue color) compared to global trends (Flemming, 1988). The orange and blue colored lines represent the regression lines for each group of sand waves. **(B)** Box and whisker plot exhibiting the minimum, maximum, median, lower, and upper quartile of the h/λ relationships for the sinuous-crested (orange) and curvilinear (blue) sand waves. **(C)** Relationship between sand wave height and lee side slope for the sinuous-crested (orange) and curvilinear (blue) sand waves.

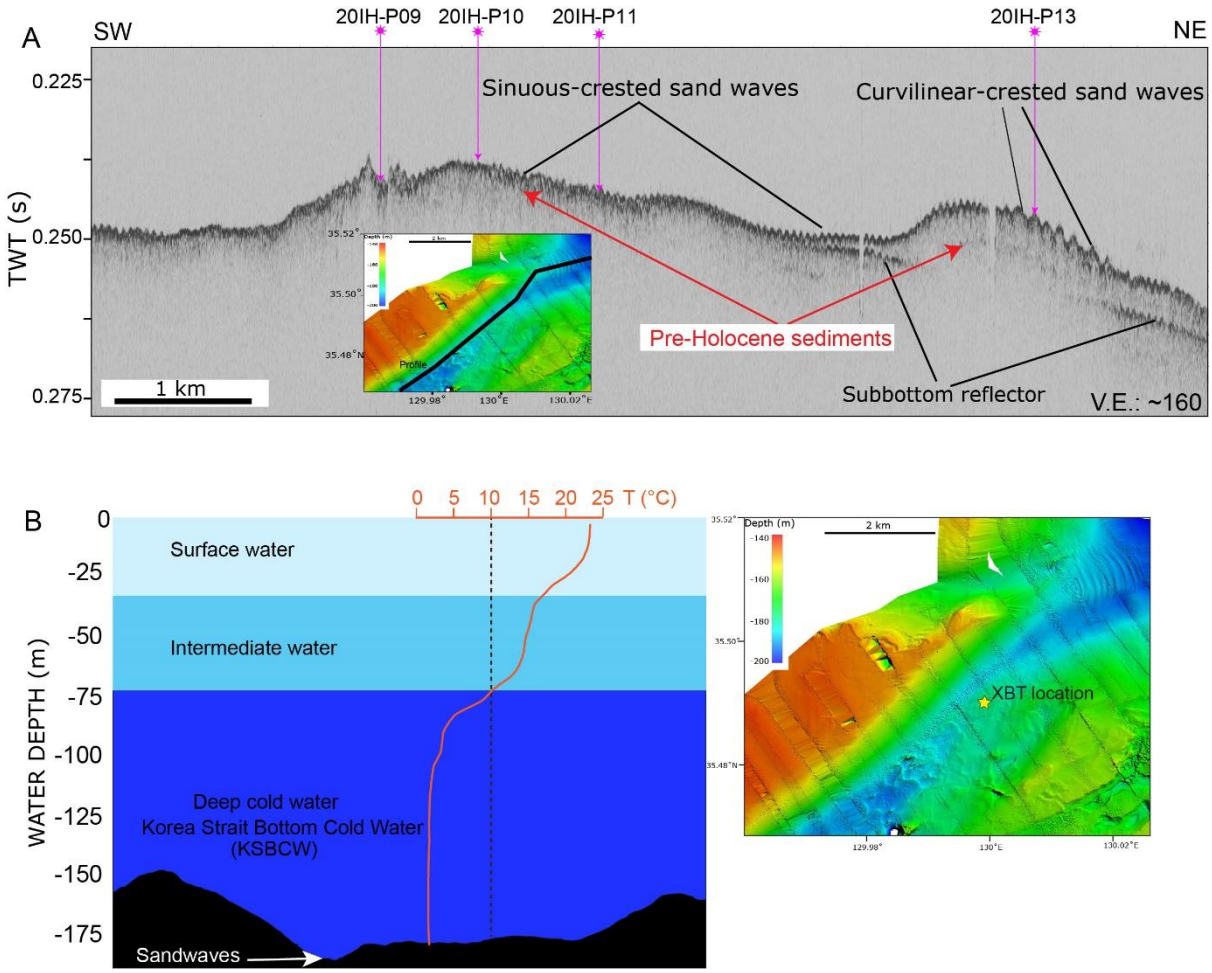

Fig. 7: (A) Subbottom chirp profile showing the seabed morphology, a distinct subbottom reflector, and sand waves on the seafloor characterized by undulating high amplitude reflectors. The subbottom reflector pinches out on the seafloor towards the SW and is interpreted as an old erosion surface. **(B)** XBT profile from the sand wave field showing a cold-water mass below 75 m water depth. The XBT profile was measured on September 17, 2020. The vertical dashed line defines water mass with less than 10°C, representing the KSBCW (Cho and Kim, 1998).

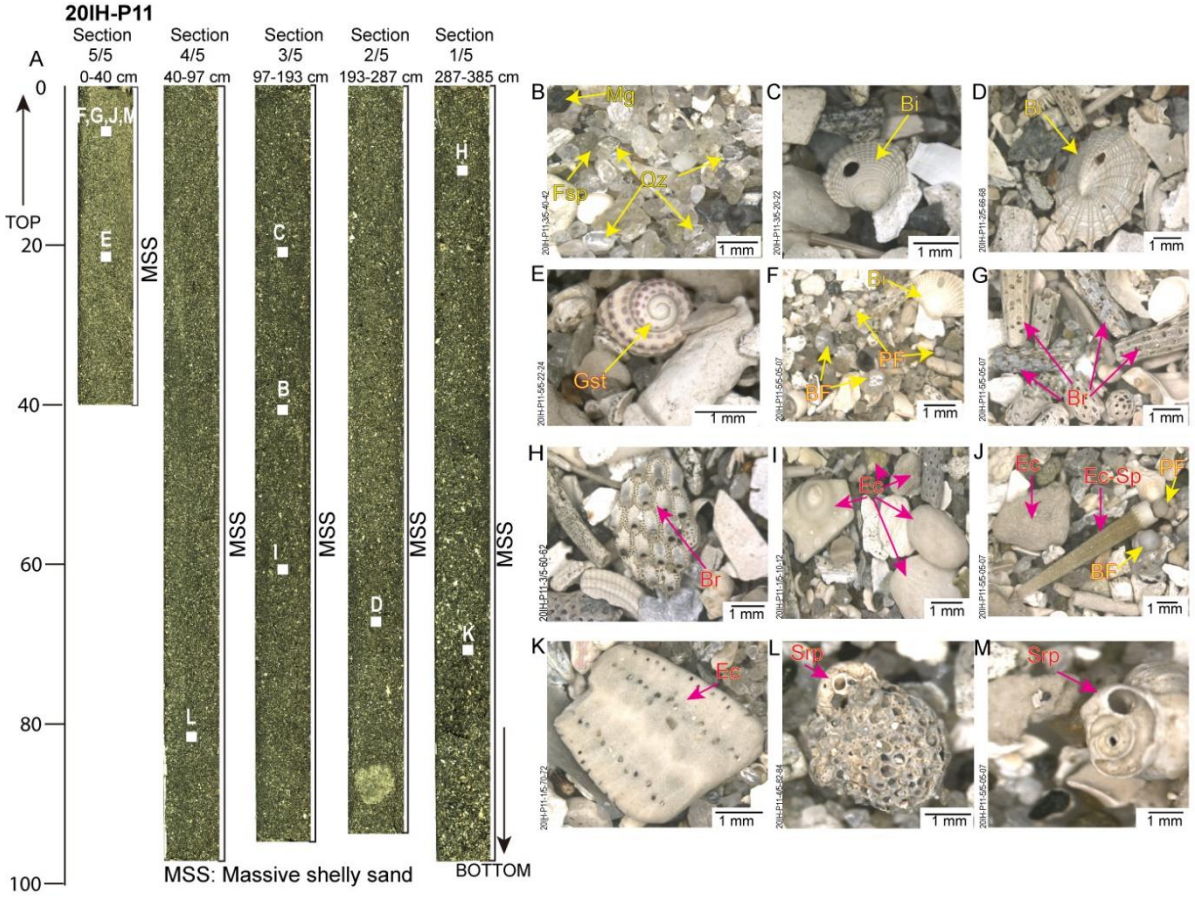

Fig. 8: (A) Core photographs obtained from piston core 20IH-P11 showing that the sediments forming the sand waves consist of massive shelly sand. (B)–(M) Selected microscopic images from core P11 showing the presence of quartz (Qz), feldspar (Fsp), magnetite (Mg), bivalves (Bi), gastropode (Gst), benthic foraminifers (BF), planktonic foraminifers (PF), bryozoans (Br), echinoderms (Ec), echinoderm-spine (Ec-Sp), and serpulids (Srp).

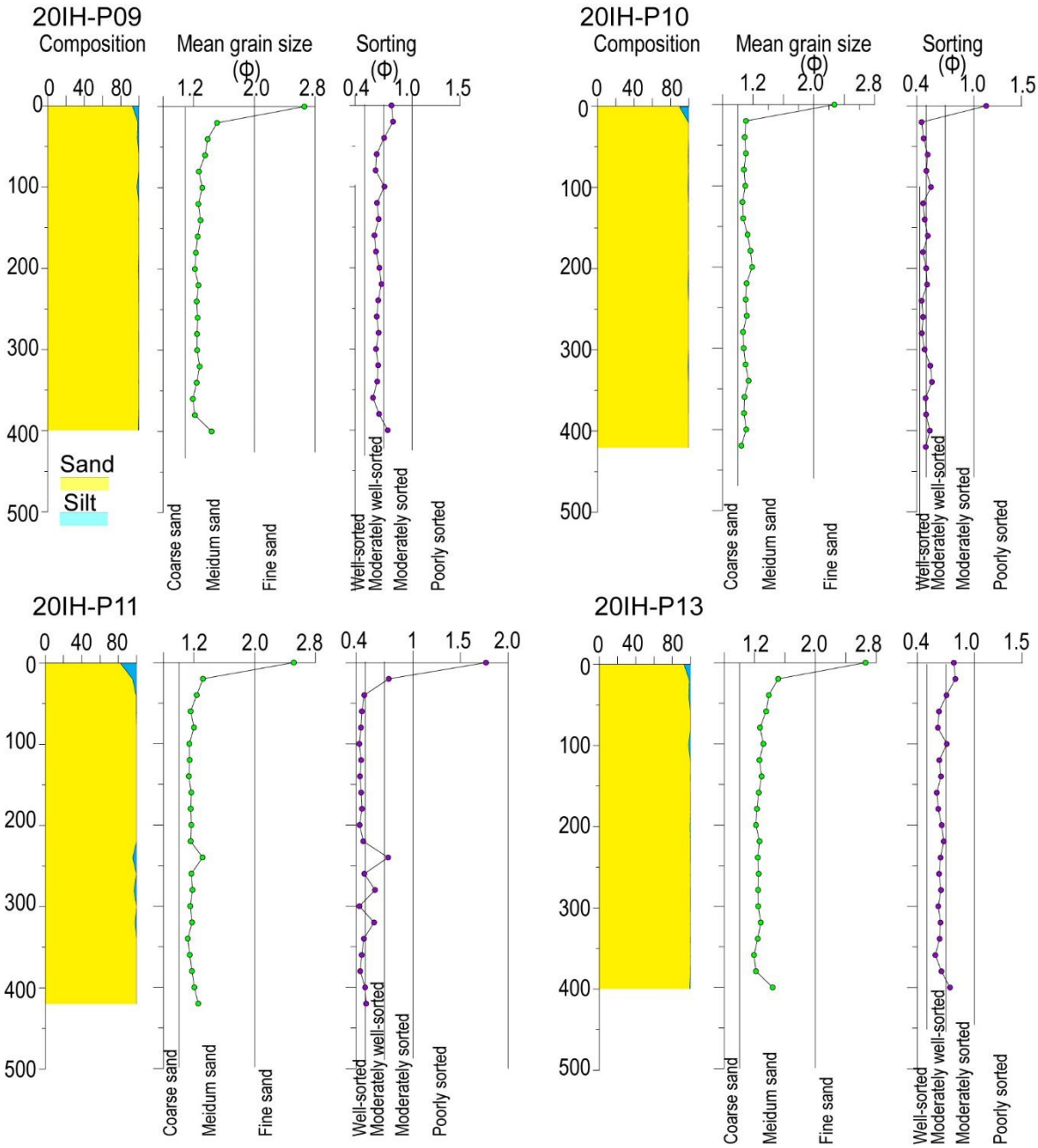

Fig. 9: Vertical profiles of volume percent, mean grain size, and sorting of the siliciclastic fraction of cored sediment retrieved from sand waves. The cored sediment primarily consists of well-sorted to moderately well-sorted, medium-grained sand, capped by a thin layer of more fine grained, less well-sorted sediment.

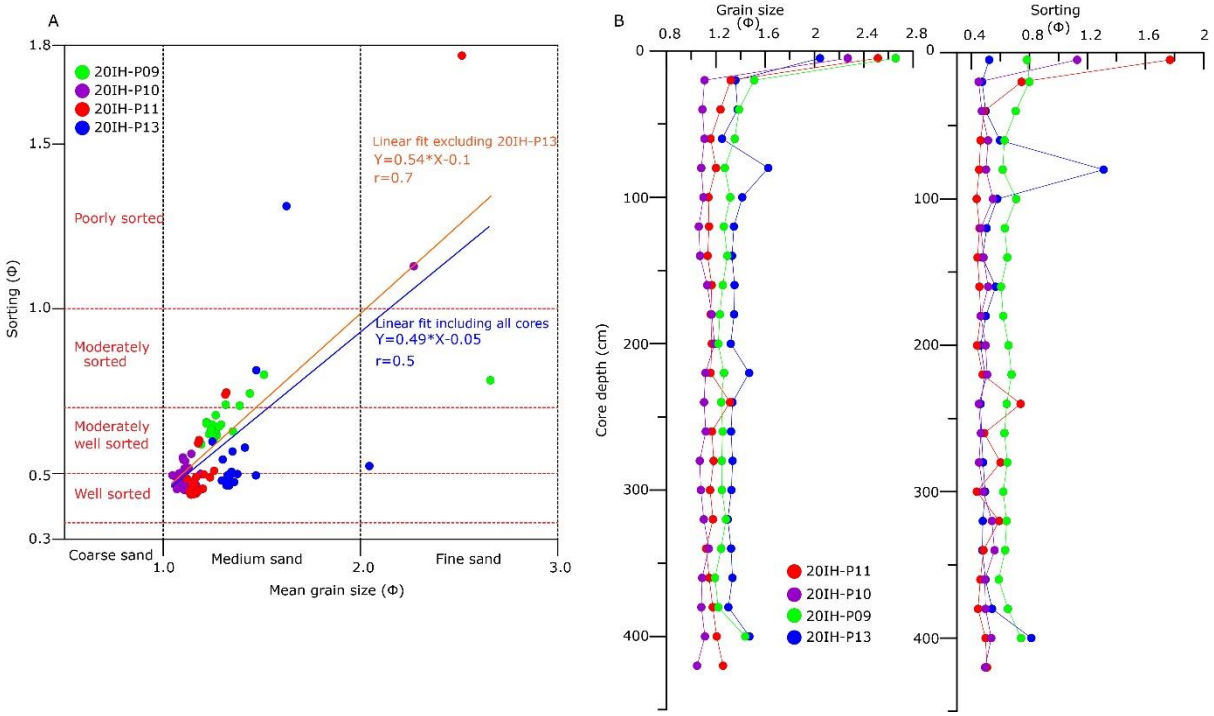

Fig. 10: (A) Scatter diagram of mean grain size versus sorting showing a linear trend between the two parameters, with sorting decreasing as mean grain size decreases. All cores exhibit better sorting in the coarser grain sizes. **(B)** Plots showing some lateral variability in grain size and sorting at each locality. P10 and P11 have larger grain sizes, suggesting deposition by stronger currents.

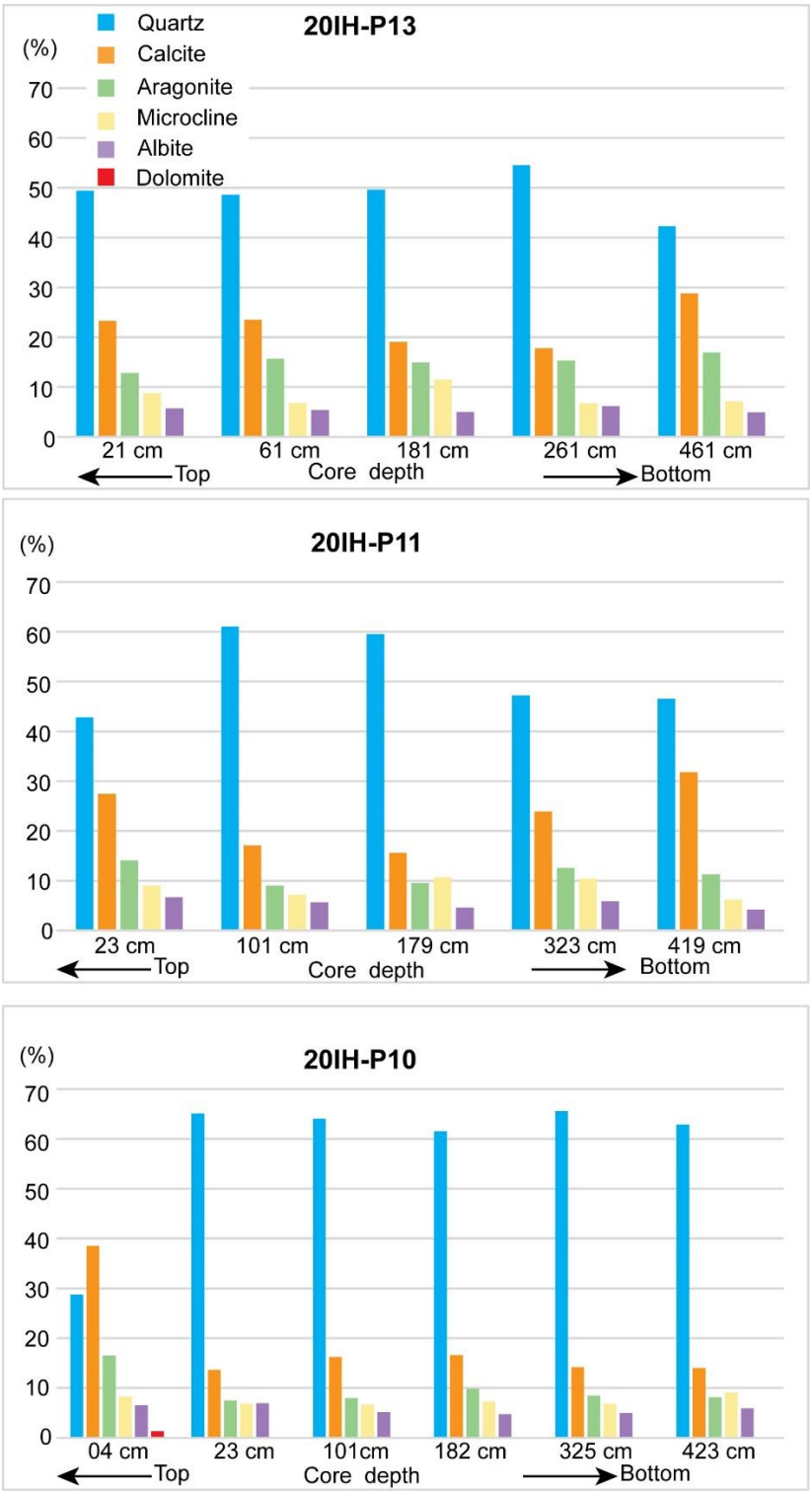

Fig. 11: Average mineral composition of selected samples from the sand waves. Six mineral types were identified, including quartz, calcite, aragonite, microcline, albite, and dolomite. Overall, the composition of sand waves is similar. Quartz is the most abundant mineral (mean: > 40%). The carbonate fraction (aragonite+calcite) contributes >35 %. Siliciclastic fraction (quartz+microcline+albite) is inversely proportional to the carbonate fraction (calcite+aragonite+dolomite).

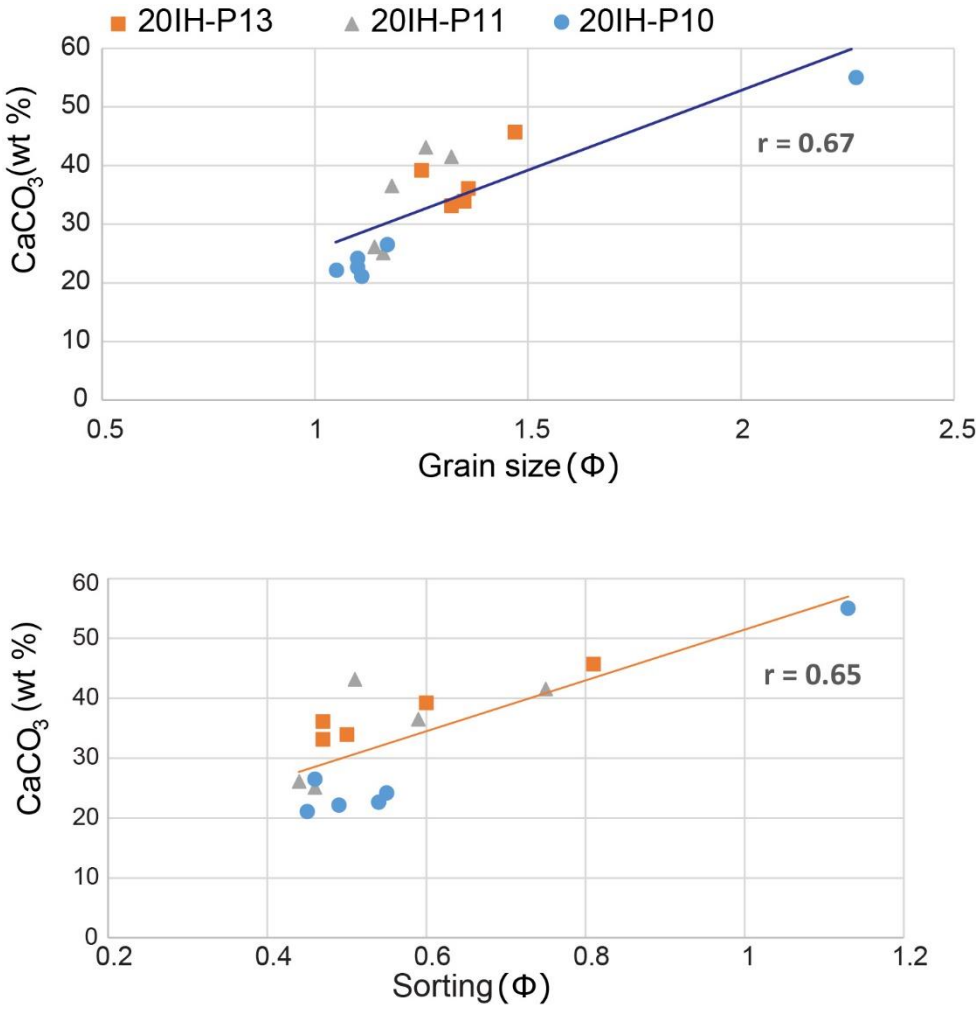

Fig. 12: Scatter diagrams of $CaCO_3$ versus grain size and sorting. The grain size and sorting of the siliciclastic fraction are correlated to the $CaCO_3$ abundance in the cores, suggesting a compositional control on the grain size.

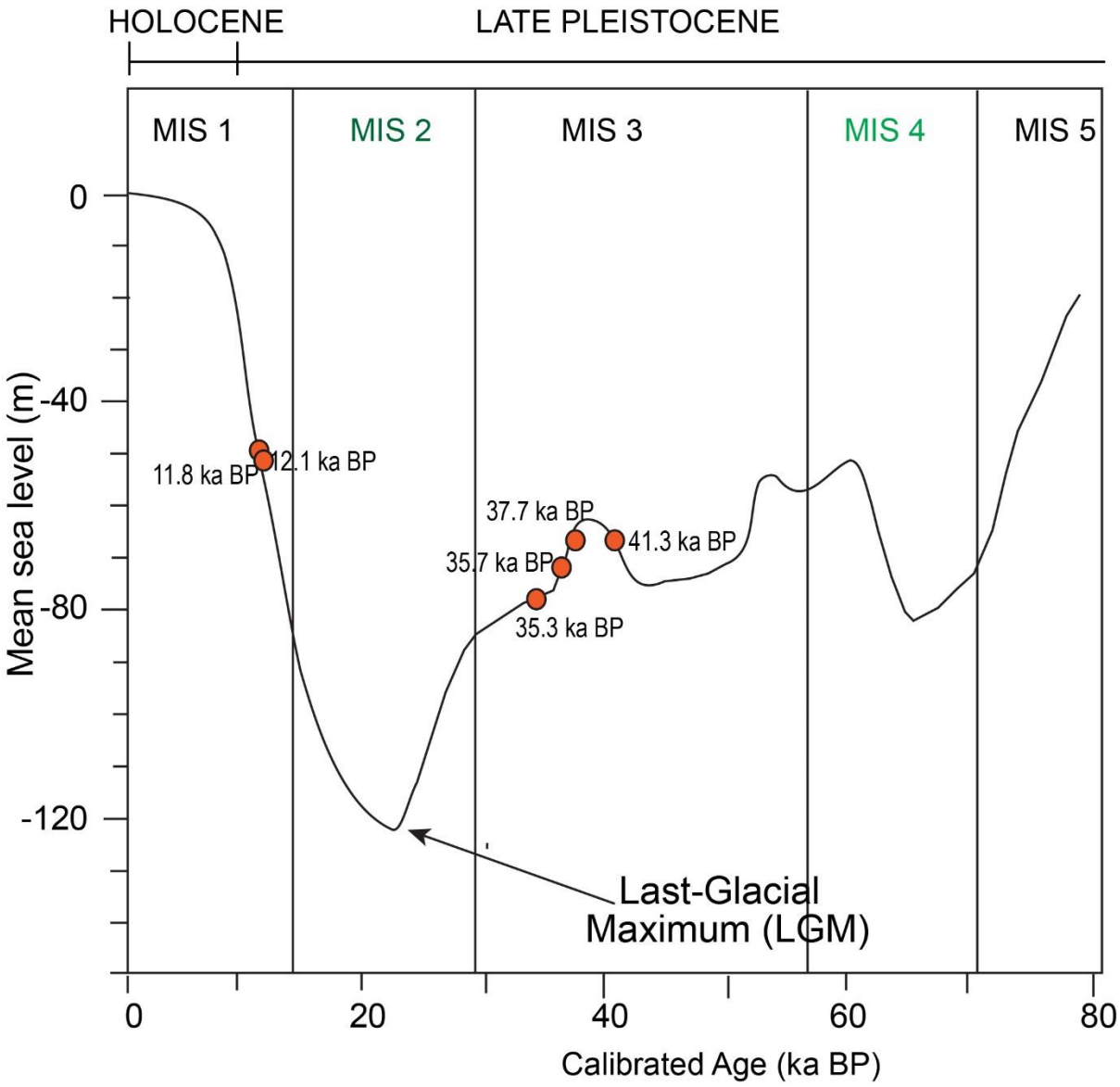

Fig. 13: Sea-level curve during the late Pleistocene (after Stanford et al., 2011; Waelbroeck et al., 2002) with the dated fossils plotted on the curve. The fossils retrieved from the sand waves are older than ~12 ka BP and were deposited when sea level was substantially lower than present.

TABLES

Table 1: Radiocarbon ages of core sediments obtained from the sand waves on the southeastern shelf of Korea. The samples were dated at the Korea Institute of Geoscience and Mineral Resources (KIGAM).

Core	Longitude(E)	Latitude(N)	Sample name	Sampling depth(m)	Dated fossils	Age yrBP	Sample code
20IH-P11	129.9962	35.4920	20IH-P11 (5/5) 5-7cm	0.06	bivalve	35653 ± 270	KGM-ICa200091
20IH-P11			20IH-P11 (2/5) 78-80cm	3.13	bivalve	37723 ± 328	KGM-ICa200090
20IH-P11			20IH-P11 (1/5) 88-90cm	4.17	bivalve	41325 ± 425	KGM-ICa200088
20IH-P11			20IH-P11 (1/5) 75-80cm	4.05	echinoderm	11843 ± 63	KGM-ICa200089
20IH-P13	130.0171	35.5097	20IH-P13 (4/4) 18-20cm	0.19	bivalve	12123 ± 52	KGM-ICa200093
20IH-P13			20IH-P13 (1/4) 45-47cm	3.60	bivalve	35276 ± 289	KGM-ICa200092

Table 2: Summary of bedform geometric properties

Bedform	Measurement	Mean	Max.	Min.
Sinuous-crested sand waves *(n=102)*	Height (m)	0.8	2.1	0.2
	Wavelength (m)	22	45	10
	Lee side slope (°)	12	20	2
Curvilinear-crested sand waves *(n=9)*	Height (m)	2	3	1
	Wavelength (m)	98	140	60
	Lee side slope (°)	2.4	4	1

Table 3: Bryozoan species from the sand waves on the southeastern continental shelf of the Korean Peninsula

	species	Distribution	Water form
1	*Heteropora japonica* Androsova, 1965	-Russia (recent: Sakhalin, Vladivostok, -25 m)	Cold
2	*Microporina japonica* Canu & Bassler, 1929	-Japan (recent: Tsugaru Strait and Boso Peninsula in Honshu) -Japan (fossil: Jizodo Fm in Honshu)	warm
3	*Leieschara subgracilis subgracilis* (d' Orbigny, 1853)	-NW Atlantic, Arctic (recent) -Japan (fossil: Kuromatsunai in Hokkaido)	cold
4	*Escharoides hataii* Hayami, 1975	-Japan (fossil: Kuromatsunai in Hokkaido)	cold